Renewable Energy 150 (2020) 293–306

Contents lists available at ScienceDirect

Renewable Energy

journal homepage: www.elsevier.com/locate/renene

The effect of support on Pd_1Nb_1 electrocatalysts for ethanol fuel cells

Felipe M. Souza [a], Julio Nandenha [b], Vitor H.A. Oliveira [a], Edson C. Paz [a], Victor S. Pinheiro [a], Luci R. Aveiro [a], Luanna S. Parreira [c], Júlio C.M. Silva [d], Bruno L. Batista [a], Almir O. Neto [b], Mauro C. Santos [a, *]

[a] Laboratório de Eletroquímica e Materiais Nanoestruturados (LEMN) – Centro de Ciências Naturais e Humanas (CCNH), Universidade Federal do ABC (UFABC). Rua Santa Adélia 166, Bairro Bangu, 09210-170, Santo André, SP, Brazil
[b] Instituto de Pesquisas Energéticas e Nucleares (IPEN), CNEN/SP. Avenida Prof. Lineu Prestes 2242, Cidade Universitária, 05508-000, São Paulo, SP, Brazil
[c] Instituto de Química (IQ), Universidade de São Paulo (USP), Avenida Prof. Lineu Prestes 748, Cidade Universitária, 05508-000, São Paulo - SP, Brazil
[d] Instituto de Química da Universidade Federal Fluminense, Grupo de Eletroquímica e Materiais Nanoestruturados, Campus Valonguinho, CEP, 24020-141, Niterói, RJ, Brazil

ARTICLE INFO

Article history:
Received 24 May 2019
Received in revised form
21 November 2019
Accepted 23 December 2019
Available online 2 January 2020

Keywords:
Alkaline direct ethanol fuel cell
Ethanol oxidation reaction
Palladium
Niobium
Sol-gel method

ABSTRACT

Pd_1Nb_1/C on different kinds of carbon black were prepared by a modified sol-gel method. The alkaline direct ethanol fuel cell (ADEFC) performance was performed first with the Pd_1Nb_1 electrocatalysts and then by varying the fuel concentration. In CV, Pd_1Nb_1/Printex 6L (50:50 wt%) exhibited 2.2 times higher mass activity than that of the Pd/C (Alfa Aesar); their mass activities were 1300 and 590 mA mg_{Pd}^{-1}, respectively. The best performance for the ADEFC was obtained using Pd_1Nb_1/Printex 6L, which yielded a maximum power density and cell voltage of 28 mW cm^{-2} and 1.17 V, respectively. The Pd_1Nb_1/Printex 6L electrocatalyst exhibited a more negative onset potential for the CO stripping reaction. We suggest that the higher hydrophilicity (contact angle) and higher degree of disorder of Printex 6L (Raman) corroborates these results. In addition, both bifunctional and electronic effects operated on the electrocatalyst due to the presence of metal oxides and alloys of PdNb (XRD), respectively, in the synthesized electrocatalysts. Therefore, it was notable that the support has an essential role—as important as the cocatalyst—in the electrocatalytic performance.

1. Introduction

Alkaline direct ethanol fuel cells (ADEFC) are known devices for portable applications working at 30 to 70 °C and with easy operation [1].

ADEFC have noteworthy advantages related to hydrogen fuel cells [2,3]. For instance, ethanol is liquid at 298 K and 1 bar, and it is easy to store and handle. In addition, when produced from biomass, ethanol is a renewable resource, thus closing a carbon neutral cycle [4–6]. Furthermore, ADEFC have a high theoretical energy efficiency of approximately 60–90%, whereas the use of heat to generate electricity has a maximum energy efficiency of 35%. Additionally, ADEFC are mobile, which means that they do not require transmission line costs, and they have a low emission of pollutants.

Although many advances have been made in ADEFC, the major challenge in the ethanol oxidation reaction (EOR) has been the breakdown of the C–C bond [4–6]. Furthermore, the main byproducts and/or intermediates of this reaction are ethanal and acetate in alkaline media [7,8].

Palladium (Pd) is a more effective EOR catalyst in alkaline media than any other catalytic metal. However, its high cost has limited its widespread commercial use in these devices [9]. In addition, CO poisoning at the catalytic sites of Pd decreases the energy efficiency of Pd due to its long periods of use. Therefore, the use of auxiliary metals as cocatalysts proved to be promising to overcome this challenge.

There are two interesting effects from the auxiliary metals: the electronic effect and the bifunctional effect. Both effects act by facilitating the oxidation of intermediates on the surface of catalytic metals [10,11].

The results of previous studies have reported that Nb is a promising alternative metal to act as a cocatalyst of Pd in alkaline media [12]. The Nb metallic nanoparticles facilitated the oxidation

* Corresponding author.
E-mail address: mauro.santos@ufabc.edu.br (M.C. Santos).

https://doi.org/10.1016/j.renene.2019.12.110
0960-1481/

of acetaldehyde and carbon monoxide mainly by the bifunctional effect [13].

Usually, fuel cell devices use a material as a support where the metallic nanoparticles will be dispersed, and the materials typically have the following properties: high surface area, high corrosion resistance, and low electrical resistance. Carbon black (CB) is manufactured from the partial combustion or thermal decomposition of hydrocarbons in the form of gases or liquids under controlled conditions. This material has been widely used as a reinforcing agent in paints, rubbers, plastics and coatings in commercial applications for approximately 100 years [14]. Basically, this material is a fine black powder that is similar to pure elemental carbon, and it has an almost graphitic structure with low amounts of organic and inorganic compounds [15]. This minimal amount of organic material differentiates it from combustion soot [16]. In addition, CB has a characteristic particle morphology consisting of aciniform (grape-like) aggregates. In addition, depending on the origin of the carbon black, the physical and chemical properties can vary substantially [15,17].

The most widely used carbon black supports for electrocatalysts are the Vulcan XC72 and Vulcan XC72R (Cabot) [18]. Both materials have a high surface area (approximately 250 $m^2\ g^{-1}$) and a low price, and their electric conductivity is approximately 2.7 Scm^{-1}, which makes them interesting and feasible alternatives for the support of nanoparticles. Another carbon is Printex L6 (Degussa), which is a low-cost alkaline furnace pigment with a surface area of 265 $m^2\ g^{-1}$ [19], a density of 1.8 g cm^{-3}, and a high electrical conductivity [20]. However, even though they possess interesting characteristics for nanoparticle support, Printex L6 is not as widely used as Vulcan XC72 carbon black.

In this way, the performance of metal electrocatalysts depends strongly on the support material characteristics. Since the nanoparticles are distributed on the support surface, the electron transfer resistance and the chemical environment of the reaction site directly affect the efficiency of the electrocatalytic activity of an electrocatalyst [21]. For the reasons noted above, the study of these different types of carbon blacks in electrocatalysts to ADEFC is important [22].

In this work, we present PdNb binary electrocatalysts at a ratio of 1:1 of mass, which are supported by different kind of black carbon synthesized by the sol-gel method. The comparative study for ethanol oxidation reaction and ADEFC experiments in this paper will contribute to clarifying the importance of support in heterogeneous catalysis, since carbon black is usually 80% of the composition of the electrocatalysts.

2. Materials and methods

2.1. Preparation of the electrocatalysts

A modified sol-gel method was used to synthesize the PdNb/C materials [23], Briefly, the electrocatalysts were synthesized by a modified sol-gel method [23]. For this, Pd-acetylacetonate (99% Sigma-Aldrich, product by USA) and $NbCl_5$ (99% Sigma Aldrich, product by Germany) were mixed with 6 mL of isopropyl alcohol (Synth) and 2 mL of acetic acid (Synth). Next, Vulcan XC72R, Vulcan XC72 or Printex 6L carbon black was added. The sol-gel solution was homogenized by magnetic stirring and then heated for 60 min until dry. The samples were submitted to heat treatment in a muffle furnace under a N_2 atmosphere. The samples were heated at 5 °C min^{-1} in two steps. First, the samples were heated from room temperature to 110 °C, and this temperature was maintained for 15 min. Then, the samples were heated from 110 °C to 400 °C, and this temperature was maintained for 60 min. After the heat treatment process, the samples were slowly cooled until they reached room temperature. The electrocatalyst Pd/C (Alfa Aesar) will be investigated for comparison with the synthesized ones and it was purchased by the company Alfa Aesar in the composition of 20% Pd supported on wet activated carbon.

2.2. Electrochemical measurements

2.2.1. Electrochemical cell

The catalytic activity and electrochemical characterization of the materials were performed using cyclic voltammetry (CV) and chronoamperometry (CA) with a potentiostat Autolab 302N. KOH (1.0 mol L^{-1}) was used as electrolyte in the presence or absence of ethanol (1.0 mol L^{-1}). An electrochemical cell for a three-electrode configuration was used, a platinum electrode of 1.0 cm^2 was the auxiliary electrode and a Hg/Hg_2Cl_2 (SCE) was the reference electrode and the studied electrocatalyst supported on a glassy carbon electrode with 0.5 cm^{-2} of geometric area was used as working electrode.

The system above was arranged in a 40 mL cell with N_2-degassed. The concentration of ethanol 1.0 mol L^{-1} for both CV and CA tests was used into the electrolyte solution. The temperature was the room one.

2.2.2. Preparation of the working electrode

This step is the same one as our previous publications [12,13].

2.2.3. CO-stripping analysis

The CO stripping analysis was carried out using a 1 mol L^{-1} KOH electrolyte between −0.8 V and 0.2 V, and the sweep rate was 20 mV s^{-1}. Ultra-pure N_2 (99.99%) was bubbled before the experiment through the electrolyte during 30 min. Subsequently, the working electrode was immersed into the electrolyte solution, and CO (99.9%) was purged (10 min) to form the CO monolayer onto the surface of the working electrode at −0.1 V vs. SCE. CO excess from electrolyte was removed with N_2 (99.99%) during 20 min.

2.3. Experimental characterization

2.3.1. X-ray diffraction (XRD) and BET analysis

All electrocatalysts were physically characterized using X-ray diffraction (XRD). A Rigaku-MiniFlex X-ray diffractometer with a CuKα (λ = 1.54056 Å) using a radiation source operating continuously (2° min^{-1}) from 20° to 80° (2θ) was used to both discuss about the metallic or oxide phases and the mean crystalline size estimation. The carbon materials used in this study were Vulcan XC72R, Vulcan XC72 and Printex 6L carbon black, which were purchased from Cabot. The Brunauer-Emmett-Teller (BET) surface areas of the carbon materials were measured following the procedure adopted in Ref. [24].

2.3.2. Elemental composition by ICP-MS analysis

The elemental composition of the electrocatalyst was measured using an inductively coupled plasma mass spectrometer (ICP-MS, Agilent 7900, Hachioji, Japan) operated with high-purity argon (99.9999%, White Martins, Brazil). All the conditions for these measurements were described earlier in our previous publications [12,13].

2.3.3. Energy dispersive X-ray spectroscopy (EDS)

The energy dispersive spectroscopy (EDS) analyses were performed using an EDS chemical microanalysis module that was coupled to a JSM-6010LA Compact Sweep Electron Microscope (JEOL) at an acceleration voltage of 20 kV. The EDS analyses were obtained using the map mode with twenty measurements, and the average concentration was acquired from each mapped part of the

sample. The samples of catalysts synthesized were analysed in powder form placed on a copper adhesive tape.

2.3.4. Transmission electron microscopy (TEM)

To both measure their sizes and morphology of the particles transmission electron microscopy (TEM) was carried out with a high-resolution TEM (JEOL model JEM 2100F) operating at 200 kV. Samples for TEM studies were prepared as before [12,13]. The compositional distribution (mapping) and the average particle size was performed like references [12,13].

2.3.5. Contact angle

The contact angle measurements of the Vulcan XC72, Pd/C, and PdxNbx/C-based electrocatalysts were performed using a goniometer (GBXTM digidrop) to characterize the hydrophilicity of each material studied [13].

2.3.6. Raman spectroscopy

Raman spectroscopy was carried out to study the structure of the electrocatalysts. D and G band peaks for carbon black is the main focus of this technique. The Raman spectra were recorded using a Triple T64000 Raman spectrometer (Horiba Jobin-Yvon S.A.S., France) with a microanalysis option and a CCD detector (1024 × 256—OPEN-3LD/R) with a quantum response of ~40% and a spectral resolution of 0.5 cm^{-1}. The excitation laser was 532 nm (Verdi G5, Coherent Inc., United States) and focused on a spot. The measurements were performed by using a plan achromatic 50X objective (0.20 mm/NA = 0.50). The curve fitting of the Raman spectra was obtained with the software LabSpec, and 10 spectra of the electrocatalysts were collected at different points in the samples for assignment of mean values and standard deviation of the D and G band peak. The experiments were performed according to our previous publication [38].

2.3.7. Thermogravimetric analysis (TGA)

The carbons were characterized by thermogravimetric analysis (TGA) using a LABSYS EVO STA SETARAM thermal analyzer in an alumina crucible (Al_2O_3) and argon atmosphere with a sample mass of approximately 20 mg. The heating was from 0 °C to 1600 °C, with a heating rate of 10 °C min^{-1}. The results of the measurement and discussion are available in the supplementary material.

2.3.8. Brunauer-Emmet-Teller (BET) surface area

The carbon materials used herein were Vulcan XC72R, Vulcan XC72 and Printex 6L carbon black purchased from Cabot. N_2-physisorption analysis was performed using Quantachrome Instruments Surface Area & Pore Size Analyzer with Nova 2200e software and the isotherm was measured at −196 °C. The samples were weighed, placed on the analysis port, and prior to analysis they were heated at 350 °C for 4 h under vacuum. The specific surface area data was obtained following the Brunauer-Emmett-Teller (BET) theory and the pore size distribution was obtained from t-plot method model [25].

2.4. Direct ethanol fuel cell (DEFC) experiment

2.4.1. Treatment of Nafion and membrane electrode assembly preparation

The Nafion® membranes (N117, DuPont) underwent the standard procedure for cleaning and anionic activation with successive washing steps [13]. The MEAs were prepared as before [13] in which a Pt/Vulcan XC72 (BASF) commercial cathode (1 $mg_{(Pt)}$ cm^{-2}) and either a homemade Pd_1Nb_1/carbon black anode (1 $mg_{(Pd)}$ cm^{-2}) or a Pd/C (Alfa Aesar) commercial anode (1 $mg_{(Pd)}$ cm^{-2}) at 125 °C for 420 s under a pressure of 247 kgf cm^{-2} were used. The MEA was placed between two bipolar plates and assembled in a single fuel cell [13].

2.4.2. DEFC test

The fuel cell operating performances were determined in a single DEFC with a geometric surface area of electrodes equal to 5.0 cm^2 using a test bench from the Electrocell® Group that allows control over the fuel cell operating parameters according to the previous publication [13] and the modifications carried out were inserted in the captions of Figs. 11, 12a and 12b.

3. Results and discussion

3.1. Physical-chemical characterization

3.1.1. Concentration by ICP-MS and EDS

The mass ratios of Pd and Nb for the electrocatalysts were obtained by SEM/EDS and ICP-MS analyses and are summarized in Table 1, in addition to Pd/C (Alfa Aesar). Fig. S2 shows an SEM image of the Pd/C (Alfa Aesar) electrocatalyst where the activated carbon support has a different morphology compared to the carbon black investigated. Both techniques, ICP-MS and EDS, showed similar Pd and Nb mass ratios in the electrocatalysts, which were close to the nominal mass ratio. The mass concentration values of Pd by ICP-MS were used to normalize the results of the electrocatalytic activity studies in this work. The real Pd-to-Nb atomic ratios were 48:52, 48:52 and 40:60 for Pd_1Nb_1/Vulcan XC72, Pd_1Nb_1/Vulcan XC72R and Pd_1Nb_1/Printex 6L electrocatalysts, respectively.

3.1.2. Contact angle results

The three substrates studied in this work have different hydrophilicity, and the Printex 6L carbon black is the most hydrophilic, as shown in Fig. 1. According to Fig. 1, all synthesized electrocatalysts became more hydrophilic after synthesis. The reference material Pd/C (Alfa Aesar) has a lower hydrophobicity than Pd_1Nb_1/Vulcan XC72 and Pd_1Nb_1/Vulcan XC72R and a higher hydrophobicity than Pd_1Nb_1/Printex 6L.

The intense decrease of Printex 6L hydrophobicity after the addition of Pd and Nb nanoparticles (NPs) may be related to the structure of Printex 6L relative to carbon black Vulcan. We suggest that Pd and Nb NPs were better allocated on the carbon surface, possibly due to a large number of micropores in Printex 6L.

Generally, the more hydrophilic the material is, the better it is for kinetic adsorption and dehydrogenation of H_2O molecules on the surface of the electrocatalyst [26]. When carbonic species are strongly adsorbed on Pd, hydrogen will be rapidly removed if there is a hydroxyl adsorbed (OH_{ads}) at a nearby catalytic site, which results in an increased electrical current. In contrast, to maintain the constant adsorption of OH on Pd or Nb, it is necessary that the water molecules adsorb in them and then dissociate, as described by the reaction: H_2O_{ads} (weakly adsorbed) → OH_{ads} + H^+ + e^- [36]. The reaction that follows this bifunctional mechanism is $Pd\text{-}CO_{ads} + 2Nb\text{-}OH_{ads} \rightarrow CO_2 + H_2O + Pd + Nb$, where the formed $Pd\text{-}OH_{ads}$ or $Nb\text{-}OH_{ads}$ favors the oxidation of $Pd\text{-}CO_{ads}$. Therefore, the hydrophilicity of an electrocatalyst plays an important role in heterogeneous catalysis.

3.1.3. Raman spectroscopy results

The Raman spectra of the electrocatalysts (Figs. 2 and 3) show the well-known peaks of the D-band at 1350 cm^{-1} and the G-band at 1580 cm^{-1} for carbon black [27]. The vibrational D-band is associated to the relaxation movement of the hexagonal carbon network and the existence of structural disorder [28]. The G-band is essentially caused by vibration and stretching in the plane of the sp^2 carbon [29]. The ratio between the intensities of the I_D/I_G bands

Table 1
Pd and Nb concentrations (mass ratios) determined by using ICP-MS and EDS.

Electrocatalyst	Pd nominal (%)	Pd ICP-MS (%)	Pd EDS (%)	Nb nominal (%)	Nb ICP-MS (%)	Nb EDS (%)
Pd_1Nb_1/Vulcan XC72	10	9.5 ± 0.004	9.8 ± 1.4	10	9.0 ± 0.05	9.3 ± 0.4
Pd_1Nb_1/Vulcan XC72R	10	9.6 ± 0.013	9.9 ± 0.8	10	8.8 ± 0.14	9.4 ± 0.9
Pd_1Nb_1/Printex 6L	10	7.4 ± 0.002	9.6 ± 0.6	10	9.8 ± 0.11	8.7 ± 0.5
Pd/C (Alfa Aesar)	20	21.9 ± 0.005	22.7 ± 1.8	n.d.	n.d.	n.d.

n.d. = Not determined.

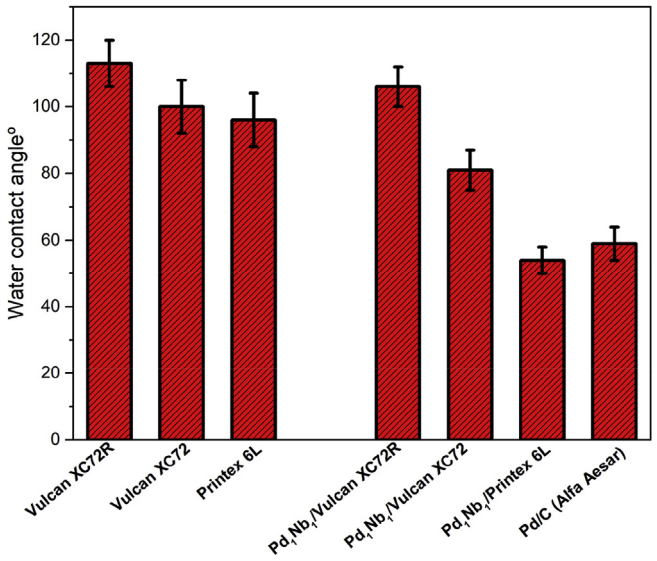

Fig. 1. Hydrophilicity results from the contact angle tests.

leading information on the number of defects in the material [30]. Therefore, high values indicate a greater number of defects in the structure of the hexagonal carbon, and low values indicate a lower number of defects. In Fig. 2, we see that the Printex 6L support has the highest I_D/I_G ratio. This difference in defects in the structure of Printex 6L is possibly due to the presence of a greater number of oxygenated functional groups in the carbon structures [27]; this condition reinforces the contact angle results, which showed that this material had the highest hydrophilicity.

After synthesis, all carbon supports increased the I_D/I_G ratio, as shown in Table 2. These results were expected because we inserted NPs on the hexagonal carbon structures, which generated a greater number of defects. In Fig. 3, we can see how the D-band increased for the synthesized electrocatalysts and how the Pd/C also has an I_D/I_G ratio greater than 1. In addition, we see that Pd_1Nb_1/Printex 6L has a substantially superior I_D/I_G ratio in comparison to those of the other electrocatalysts in this study, as shown in Table 2.

The greater the increase in the degree of structural disorder of carbon black, the more points that are created in the structure that are similar to graphene. In this way, carbon black becomes less resistive, and the electron-transfer rate increases between the electrode interface and solution [30–32].

3.1.4. Brunauer-Emmet-Teller (BET) surface area results

The N_2 adsorption-desorption technique allows the assessment of the textural properties of porous materials by using N_2 as a probing molecule [33]. BET surface area experiments were taken from the catalyst supports to first estimate the surface area of the carbon supports used in this work, and the results are shown in Table 3. The literature reports specific surface area values (S_{BET}) for the Vulcan XC72R, Vulcan XC72 and Printex 6L carbon supports as 241, 230 and 265 $m^2\ g^{-1}$, respectively. In this way, the carbon blacks used in this study are close to those reported in the literature [22,28].

The Printex 6L support material has a higher surface area than that of Vulcan XC72R or Vulcan XC72 (Table 3). In addition, Printex 6L had a higher volume of micropores than other carbon blacks (Table 3). Activated carbons with high surface area usually have a high volume of micropores, given that micropores have a high surface area-to-volume ratio [34]. In this way, the micropores have a greater contribution to the superficial area of the material than that of mesopores or macropores [35]. Besides, the micropores play an important role in processes based on adsorption, as in the case of adsorption of water, oxygen and ethanol molecules (small molecules) [34]. Finally, the micropores are related to adsorbent-adsorbate affinity because adsorbent molecules are forced against the walls of the micropore [36]. These properties of electrocatalyst microporosity are interesting for heterogeneous catalysis.

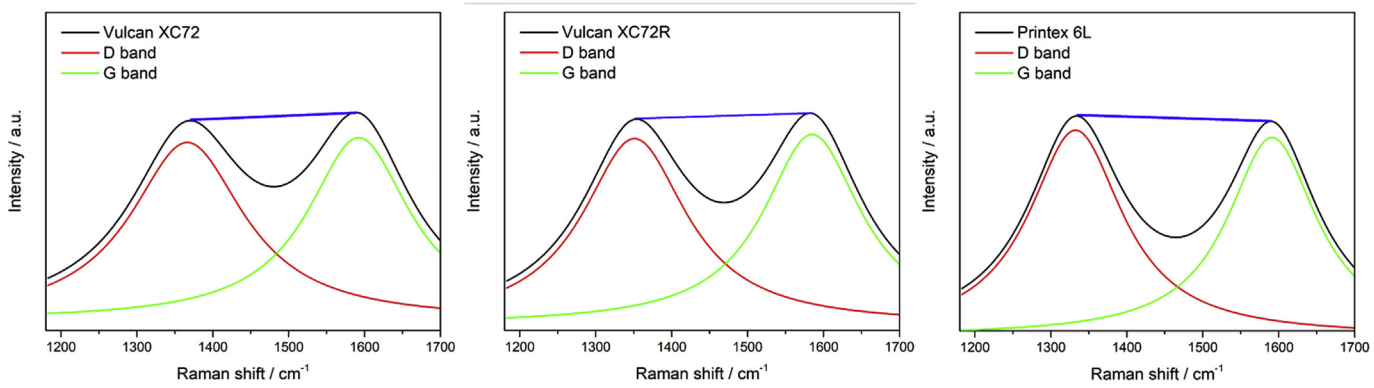

Fig. 2. Raman spectra of the carbon black supports.

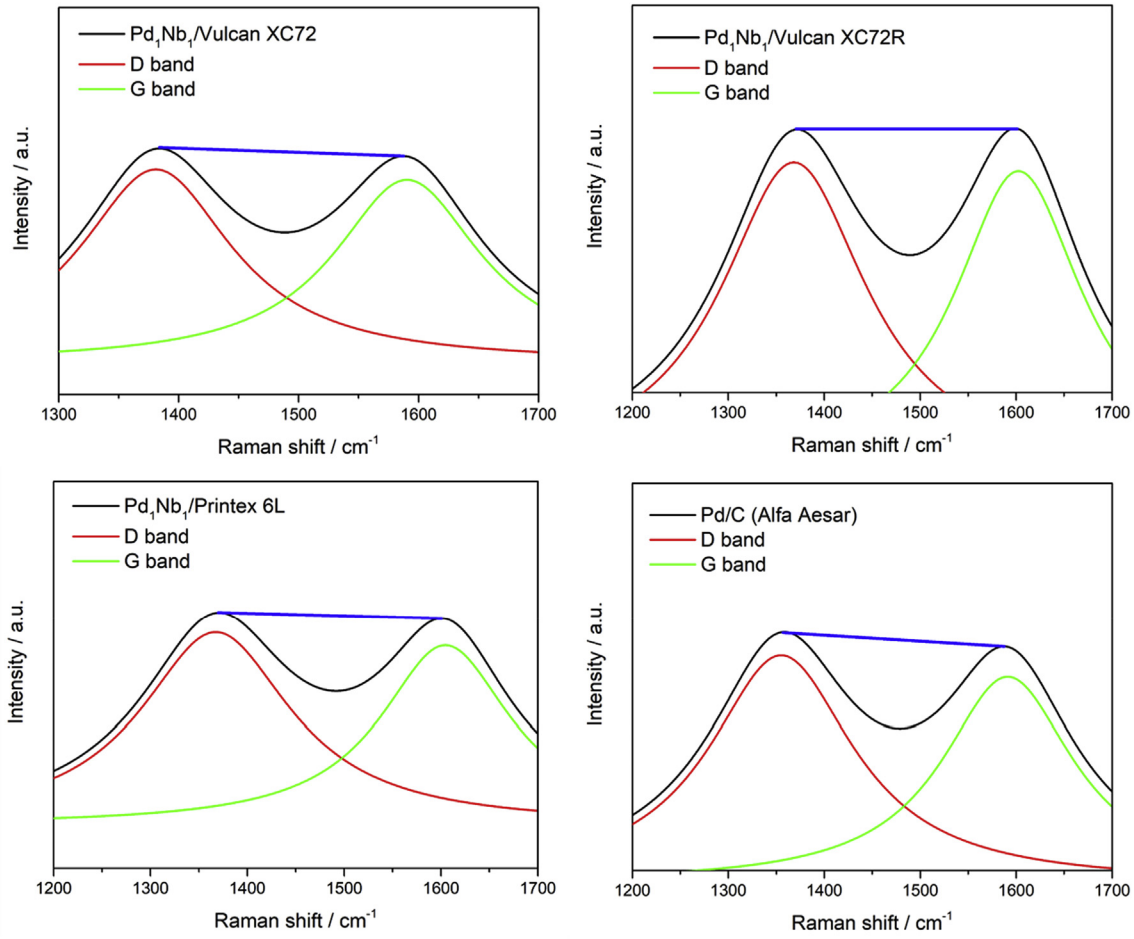

Fig. 3. Raman spectra of the electrocatalysts.

Table 2
The ratio of the D/G bands integrated from the Raman spectra.

Materials	I_D/I_G ratio
Printex 6L	1.06 ± 0.01
Vulcan XC72	0.98 ± 0.01
Vulcan XC72R	0.98 ± 0.008
Pd_1Nb_1/Printex 6L	1.08 ± 0.03
Pd_1Nb_1/Vulcan XC72	1.01 ± 0.02
Pd_1Nb_1/Vulcan XC72R	1.01 ± 0.01
Pd/C (Alfa Aesar)	1.02 ± 0.005

Table 3
Physical properties of the carbon supports.

N_2 adsorption-desorption	Vulcan XC72R	Vulcan XC72	Printex 6 L
S_{BET} ($m^2\ g^{-1}$)	226	236	255
Pore Volume (cc g^{-1}) V_{total}	0.20	0.22	0.18
V_{meso}	0.18	0.19	0.12
V_{micro}	0.02	0.03	0.06

S_{BET} = specific surface area BET.

3.1.5. X-ray diffraction results

The X-ray diffractograms presented in Fig. 4 show the presence of a mixture of metallic and oxidized Pd in the synthesized electrocatalysts and in Pd/C (Alfa Aesar). These crystallographic structures are in the XRD pattern database called the Joint Committee on Powder Diffraction Standards (JCPDS) with codes 46–1043 and 41–1107 for Pd and PdO, respectively [13]. The Pd is in the face-centered cubic (fcc) crystalline system with a typical Cu-fcc structure [37], and the PdO is in the tetragonal crystalline system with a typical paladinite structure [38].

Although the presence of crystalline Nb faces was not detected, it is possible to verify that there is a displacement in the peaks of Pd to lower values for the electrocatalysts with Nb in the structure. The XRD technique was unable to detect Nb because it is in an amorphous form adsorbed on carbon. The sol-gel method used naturally results in the species a-Nb_2O_5 (amorphous Nb_2O_5), to obtain the other polymorphic forms of Nb_2O_5 a controlled hydrothermal process is required [39]. We suggest that this well-known form in the literature is present in electrocatalysts. There are some reports that report this amorphous condition of Nb that does not allow XRD detection [40,41]. However, it is present in an amount like Pd as evidenced by ICP-MS. In addition, there is a broad peak that is centered at about $2\theta = 25°$ (Bragg angle), which is well known to be from the reflection plane (002) of the hexagonal structure of the carbon black support [42].

The average crystallite size was estimated using the Scherrer formula [12] and was calculated from the full width at half maximum (FWHM) of the peak (1 1 1) at $2\theta = 40°$ for all electrocatalysts because it is a peak with less interference than the broad peak of semicrystalline carbon. The average crystallite sizes for the Pd/C (Alfa Aesar), Pd_1Nb_1/Printex 6L, Pd_1Nb_1/Vulcan XC72R and Pd_1Nb_1/Vulcan XC72 electrocatalysts were 0.9, 2.3, 3.4 and 4.7 nm, respectively. This sequence suggests that the mean crystallite sizes

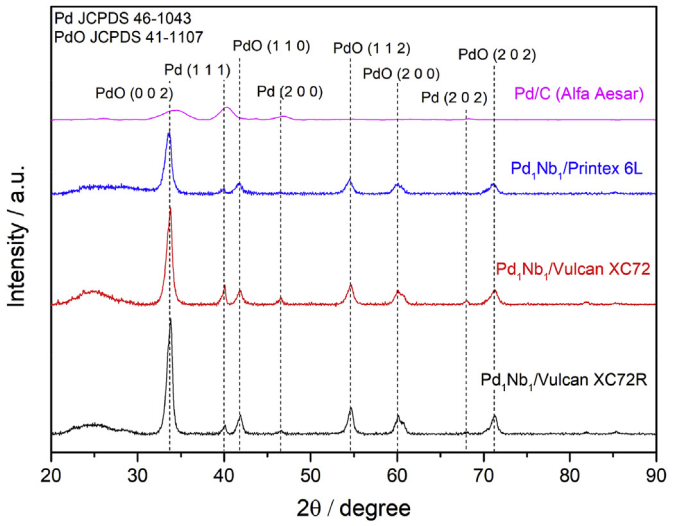

Fig. 4. X-ray diffraction patterns for the electrocatalysts.

of nanoparticles (NPs) prepared are larger than the Alfa Aesar© Pd NPs.

The interplanar distance and the lattice parameter were calculated using the peak pattern for Pd (1 1 1) in the Bragg's law [43] equation to determine the interplanar spacing and the standard formula for the cubic crystal system [12]. The results in Table 4 indicate that the addition of Nb promoted increased lattice parameter however this increase was not so significant as to be strong evidence of alloy formation.

3.1.6. Transmission electronic microscopy results

Fig. 5 shows TEM images and histogram of the particle size distribution of the electrocatalysts. The spheres with a darker contrast are the metallic NPs, while the pattern of sinuous lines with the lighter contrast is the carbon black backing. From a large group of images, the metallic NPs of Pd are spherical and are sometimes elongated due to the close proximity of Nb. The electrocatalyst showed a random distribution of NPs on the carbon support; the average particle diameter was approximately 2–20 nm. As shown in Fig. 5, the particle diameters of the carbon blacks in increasing order is as follows: Pd/C < Pd_1Nb_1/Printex 6L < Pd_1Nb_1/Vulcan XC72 < Pd_1Nb_1/Vulcan XC72R. Again, the NPs with Nb have a larger average particle diameter than without Nb, which is in according with the estimation of mean crystallite size by the XRD results.

Fig. 6a presents a STEM-DF image of the Pd_1Nb_1/Printex 6L electrocatalysts. Based on the elemental mapping by XEDS (Fig. 6b and d), it is possible to see how the Nb and Pd NPs are dispersed on the carbon black structures. In this case, the EDS mapping shows that Nb is spread on the carbon black support (Fig. 6b and d), whereas the Pd NPs—the brighter spherical-shaped nanoparticles—are concentrated in a delimited region (Fig. 6e). The reason Nb is scattered on carbon black is that it is in the amorphous form a-Nb_2O_5, so it is not enclosed in a crystal structure like Pd. In Fig. 6d we have evidence that Nb is in high intensity also present in the Pd region. Although it is not evidence that Nb is in the crystalline structure of Pd, it shows that Nb is also adsorbed to Pd and can act by a bifunctional mechanism [12].

In Fig. 6f, we see the Pd and Nb spectra at a point, and we see the atomic ratio of Nb to Pd of 59%–41%. These values agree with the abovementioned atomic ratio obtained by ICP-MS of the Pd_1Nb_1/Printex 6L electrocatalyst.

Table 4
Interplanar distance and lattice parameter.

Electrocatalyst	2θ	d_{hkl} (nm)	a (Å)
Pd/C (Alfa Aesar)	40.34	2.23	3.86
Pd_1Nb_1/Vulcan XC72	40.07	2.24	3.89
Pd_1Nb_1/Vulcan XC72R	40.09	2.24	3.89
Pd_1Nb_1/Printex 6L	39.83	2.26	3.91

4. Electrochemical activity studies

4.1. Electrochemical characterization of electrocatalysts

The cyclic voltammetry (CV) of electrocatalysts was studied in a 1 mol L^{-1} KOH aqueous solution at room temperature, and the results are shown in Fig. 7. All the electrocatalysts appear to have coulombic features that are similar to the Pd/C (Alfa Aesar). However, all Pd_1Nb_1 electrocatalysts showed a positive potential shift for the PdOH reduction peak compared to the Pd/C (Alfa Aesar), whose values were −334 and −344 mV vs. SCE, respectively. The distinct negative sweep behavior indicates that the electronic structure of Pd varied with the addition of Nb into the synthesized electrocatalysts. In addition, we see that the surface reactions of Pd in increasing order is as follows: Pd_1Nb_1/Vulcan XC72 < Pd_1Nb_1/Vulcan XC72R < Vulcan Printex 6L < Pd/C (Alfa Aesar). The higher Pd/C (Alfa Aesar) normalized current for surface reactions may be associated with the support material as this commercial electrocatalyst uses hydrated activated carbon as support for Pd NPs. While the preparation materials use carbon black.

These reactions are related to different electrochemical processes that are present on the Pd electrode surface. In the positive sweep (anodic sweep), the potential range between −0.8 and −0.7 V vs. SCE is due to the oxidation of the adsorbed and absorbed hydrogen [44]: $Pd - H_{abs/ads} + OH^- \rightarrow Pd + H_2O + e^-$. The peak above −0.25 V vs. SCE in the positive scan can be associated to the formation of the PdO_2 layer on the surface of the catalyst by means of this sequence of reactions [45]. First, the hydroxide ion (OH^-) is adsorbed on the surface of Pd: $Pd + OH^- \leftrightarrow Pd - OH_{ads} + e^-$. Then, the OH^-_{ads} species is oxidized with the formation of water: $Pd - OH_{ads} + OH^- \leftrightarrow Pd - O + H_2O + e^-$ [46]. The adsorption of OH^- is an important step in the oxidation process for the EOR, as discussed previously in the water contact measurement. The peak centering at −0.35 V vs. SCE can be related to the reduction of the Pd(II) oxide during the negative sweep (the cathodic sweep): $Pd - O + H_2O + 2e^- \leftrightarrow Pd + 2\ OH^-$ [47].

Therefore, this enlargement of the voltammetric profile of the surface reactions on Pd is an indication of the capacitance and the amount of Pd catalytic sites available [12,44,48]. Those reactions on the Pd surface are important in the electrocatalytic process.

4.2. Ethanol oxidation reaction (EOR) results

The cyclic voltammograms that were obtained from the ethanol oxidation reaction (EOR) on the electrocatalysts studied are shown in Fig. 8a. The mass activity for the EOR using Pd_1Nb_1/Printex 6L is 2.2 times higher than that of the Pd/C (Alfa Aesar) in cyclic voltammetry, whose values were 1300 and 590 mA mg_{Pd}^{-1}, respectively (Fig. 8a). In addition, Pd_1Nb_1/Printex 6L has a more negative onset potential of oxidation than that of the other electrocatalysts; this value is approximately −780 mV vs. SCE (Fig. 8b). When we convert to a normal hydrogen electrode (NHE) with the following formula: $E_{NHE} = E_{SCE\ (saturated\ KCl)} + 244$ mV, the E_{onset} of Pd_1Nb_1/Printex 6L becomes −536 mV vs. NHE. As a fuel cell, the cathode typically works at ~850 mV vs. NHE. Thus, DEFC applications

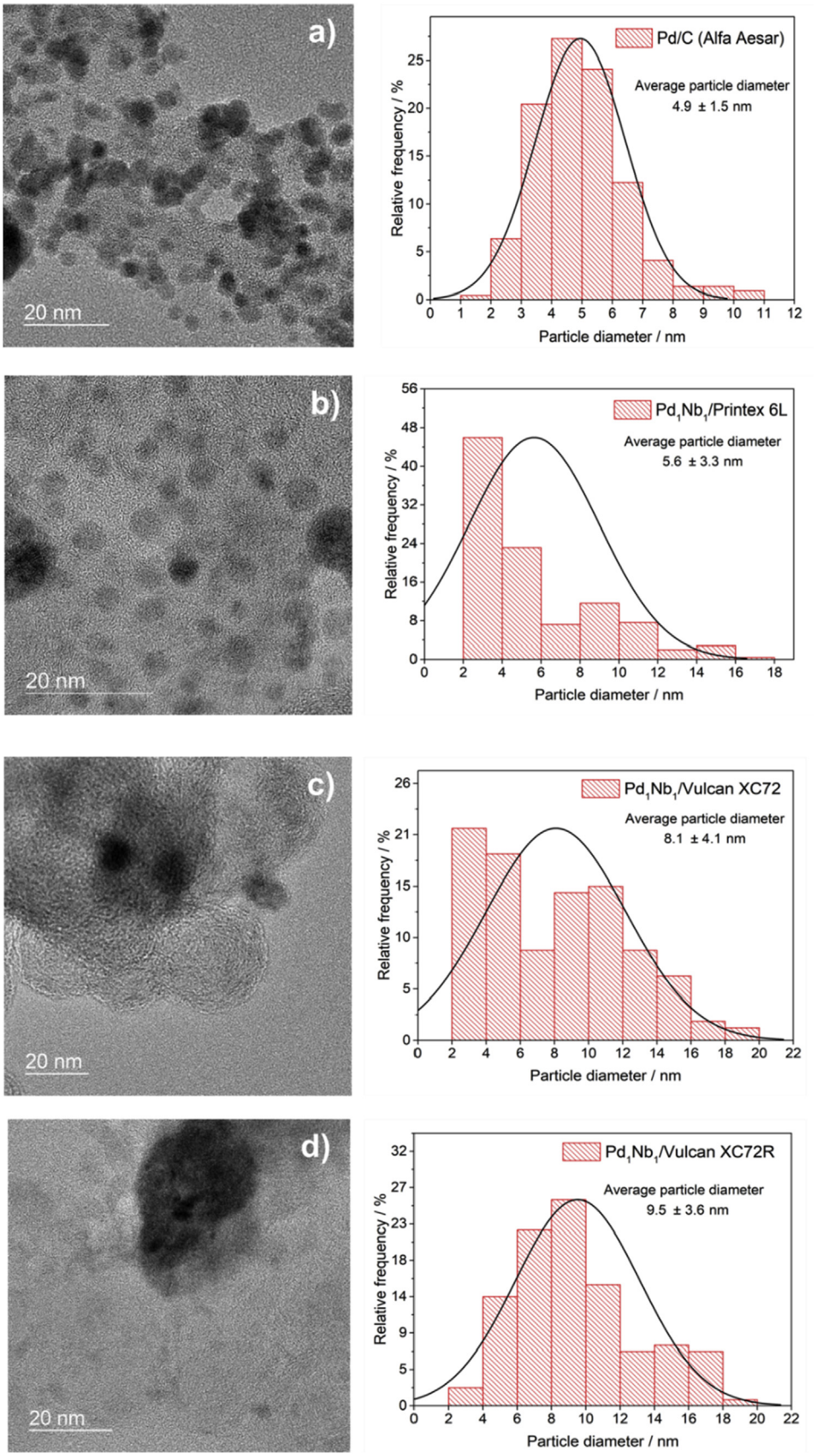

Fig. 5. TEM micrographs and particle size distribution histograms of (a) Pd/C (Alfa Aesar), (b) Pd_1Nb_1/Printex 6L, (c) Pd_1Nb_1/Vulcan XC72, and (d) Pd_1Nb_1/Vulcan XC72R electrocatalysts.

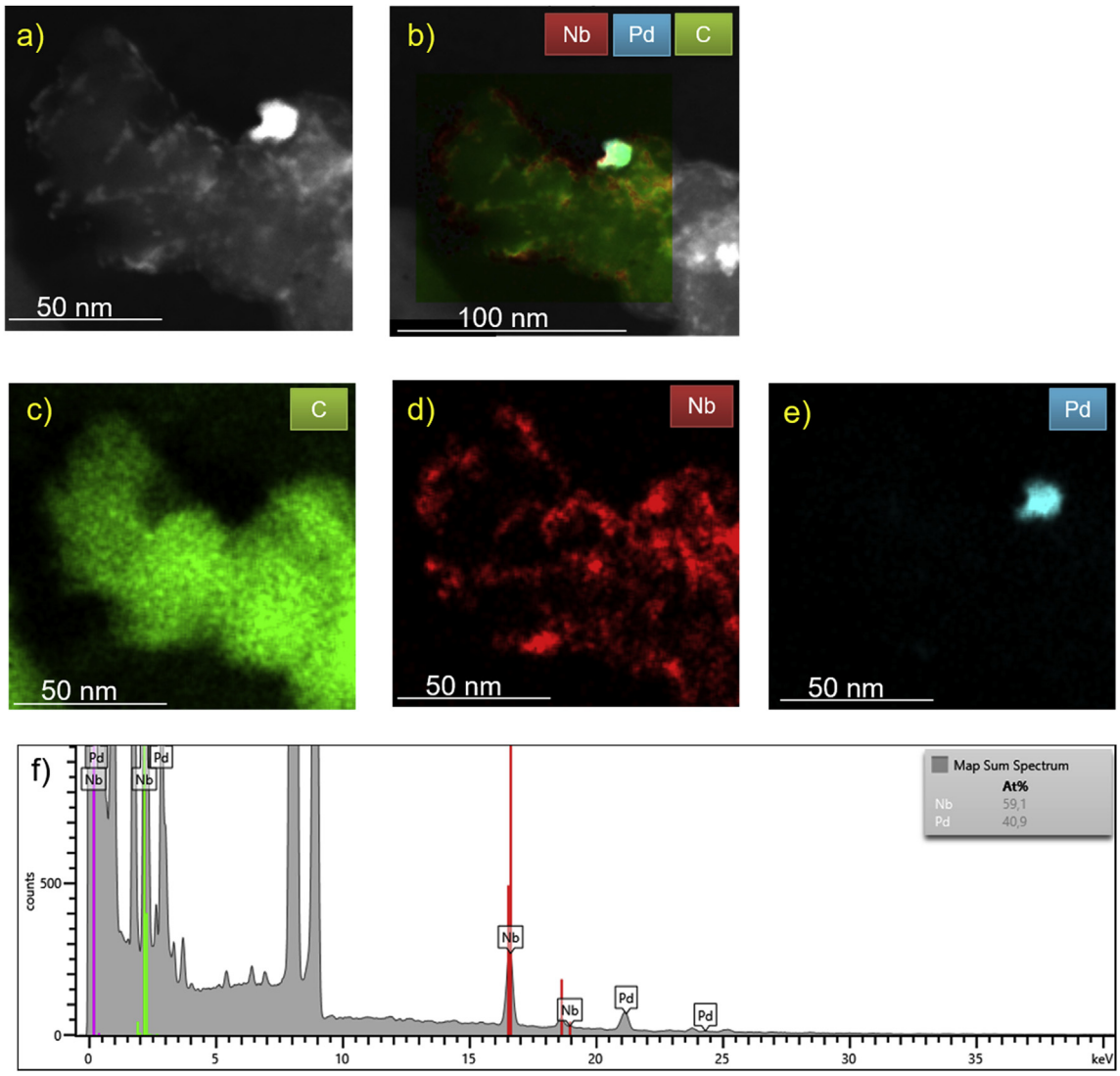

Fig. 6. TEM micrographs with EDS in a mode map showing Pd_1Nb_1/Printex 6L electrocatalysts in detail. a) Electrocatalyst image; b) RGB map; c) carbon black in the green map; d) Nb in the red map; e) Pd in the blue map; f) spectrum EDS of the point. (For interpretation of the references to colour in this figure legend, the reader is referred to the Web version of this article.)

($\Delta E_{cell} = E_{cathodic} - E_{anodic} = 0.85\ V - (-0.54\ V) = 1.39\ V$). This result suggests that in ADEFC applications, Pd_1Nb_1/Printex 6L will generate great variation in potential.

In a recent work, Moura Souza et al. [12] showed that metallic and oxidized Nb NP supports on carbon black did not presented electrocatalytic activity for the EOR.

Although Pd/C (Alfa Aesar) has the highest mass activity (approximately 43 mA mg_{Pd}^{-1}) in chronoamperometry, from 1200 s, it begins to show a more pronounced current drop than that of the Pd_1Nb_1/Printex 6L electrocatalyst (Fig. 9). This indicates that during a long oxidation period, Pd/C (Alfa Aesar) begins to be poisoned by highly adsorbed intermediates on its surface. It is worth adding that the mass activity of Pd_1Nb_1/Printex 6L (37 mA mg_{Pd}^{-1}) was 6 times and 18 times higher than that of Pd_1Nb_1/Vulcan XC72 (6 mA mg_{Pd}^{-1}) and Pd_1Nb_1/Vulcan XC72R (2 mA mg_{Pd}^{-1}), respectively, which are carbon black materials that are commonly used in electrocatalysis; these results are shown in Table 5.

We suggest that the observed improvement in electrocatalytic activity of the Pd_1Nb_1/Printex 6L electrocatalyst compared to Pd_1Nb_1/Vulcan XC72 and Pd_1Nb_1/Vulcan XC72 is related to Printex

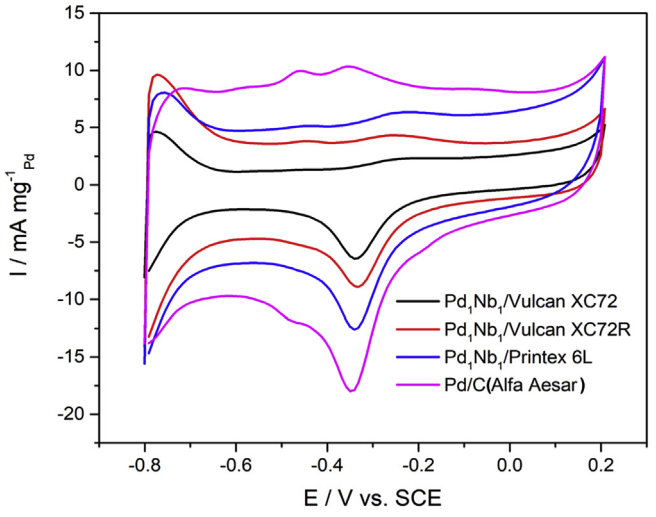

Fig. 7. Cyclic voltammograms of the electrocatalysts in 1.0 mol L^{-1} KOH at 25 °C, which were measured in a potential range from −0.80 to +0.20 V vs. SCE at a scan rate of 10 mV s^{-1}.

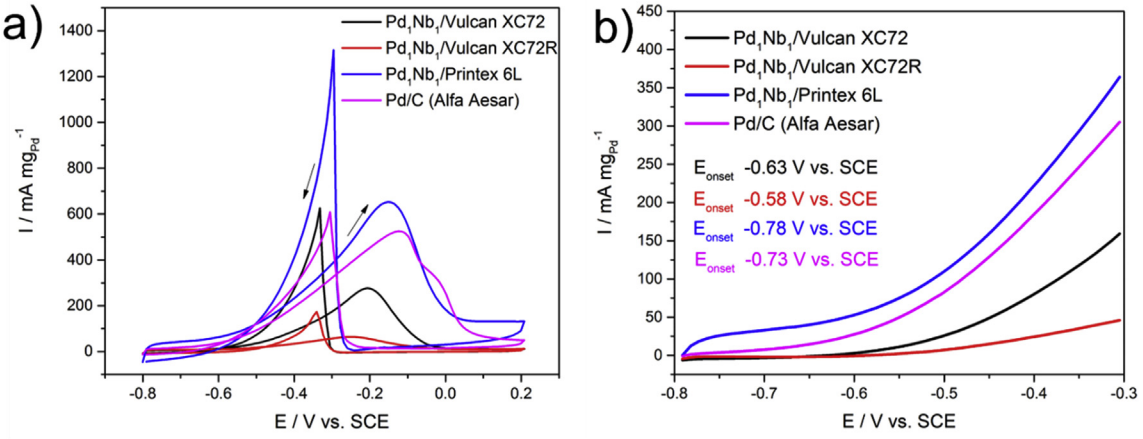

Fig. 8. Cyclic voltammograms of the Pd_1Nb_1/C electrocatalysts using 1.0 mol L^{-1} ethanol and 1.0 mol L^{-1} KOH, measured over a potential range from −0.80 to +0.20 V vs. SCE at a sweep rate of 10 mV s^{-1}.

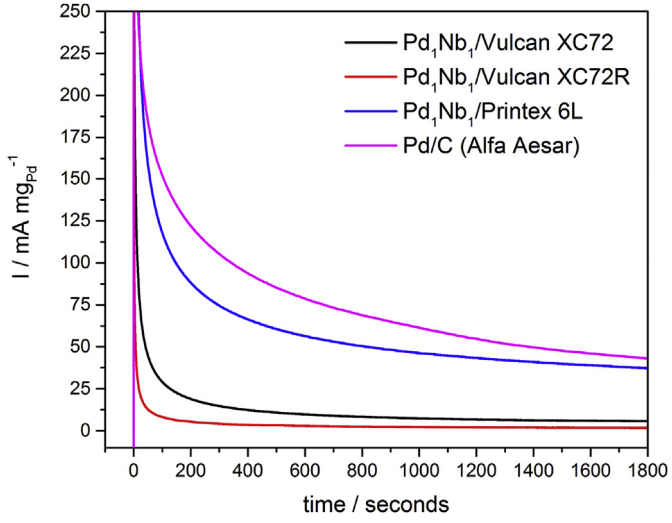

Fig. 9. Chronoamperometry at −0.40 V vs. SCE of the electrocatalysts using 1.0 mol L^{-1} ethanol in 1.0 mol L^{-1} KOH at room temperature.

6L having lower charge transfer resistance due to vacancies observed in Raman, a sized morphology. and ideal pore distribution for Pd NP location as seen in surface area analysis, higher hydrophilicity due to the higher amount of oxygenated species, etc.

4.2.1. CO-stripping results

In Fig. 10, we can see the oxidation curves of a monolayer of CO on the surface of the Pd (CO-stripping experiment). This experiment is important since one of the major challenges of ADEFC technology is the ability to oxidize and remove CO from the surface of catalytic metals [49]. We can identify that the Pd_1Nb_1/Printex 6L electrocatalyst has the most negative onset potential for CO oxidation of all the electrocatalysts studied, and it showed the highest normalized current peak per mass of Pd to oxidize CO, as shown in Fig. 10. On the other hand, even after 3 cycles of CO-stripping, Pd/C (Alfa Aesar), showed small signs of oxidation of the residual CO in the Pd, as shown in Fig. 10.

The active electrochemical surface area of the electrocatalysts was calculated from the CO-stripping experiment as before published [12]. The ECSA by CO-stripping in increasing order is Pd_1Nb_1/Vulcan XC72R < Pd_1Nb_1/Vulcan XC72 < Pd_1Nb_1/Printex 6L < Pd/C (Alfa Aesar), whose ESCA values were 1, 8, 13 and 14 $m^2\ g_{Pd}^{-1}$, respectively.

4.2.2. Direct ethanol fuel cell (DEFC) experiment

The performance of the electrocatalysts was studied in a single alkaline direct ethanol fuel cell (ADEFC). First, we performed the test for all electrocatalysts at 70 °C, which was the best temperature of the reference material in previous work [13]. Pd_1Nb_1/Printex 6L achieved the best catalytic performance, with a higher density power than Pd/C (Alfa Aesar): 42 and 31 mW cm^{-2}, respectively (Fig. 11). In this way, it is perceptive that in addition to the effect of the Nb in the electrocatalyst, the support material has a fundamental importance in the catalytic performance of the electrocatalyst. Thus, Printex 6L enhanced the electrocatalytic activity of Pd_1Nb_1 for the EOR in an alkaline medium, which supports the previous electrochemical results.

Although it is problematic to compare the results in this study with those in the literature due to the infinite number of conditions and parameters that interfere with the experimental measurements, we compare our results to some results from the literature for a similar system to this work; these comparisons are shown in Table 6.

According to Table 6, we have achieved optimum performance in this study, as we have achieved the highest open-circuit voltage (OCV) and a remarkable maximum power density (p_{max}). In

Table 5
Overview of the electrocatalytic activity results.

Electrocatalyst	[a]E_{onset} (mV vs. NHE)	Mass activity CV (**mA mg_{Pd}^{-1}**)	Mass activity CA (**mA mg_{Pd}^{-1}**)
Pd_1Nb_1/Printex 6L	−583	1300	37
Pd/C (Alfa Aesar))	−486	590	43
Pd_1Nb_1/Vulcan XC72	−386	611	6
Pd_1Nb_1/Vulcan XC72R	−336	174	2

[a] Conversion of SCE to NHE by: $E_{NHE} = E_{SCE\ (saturated\ KCl)} + 244$ mV.

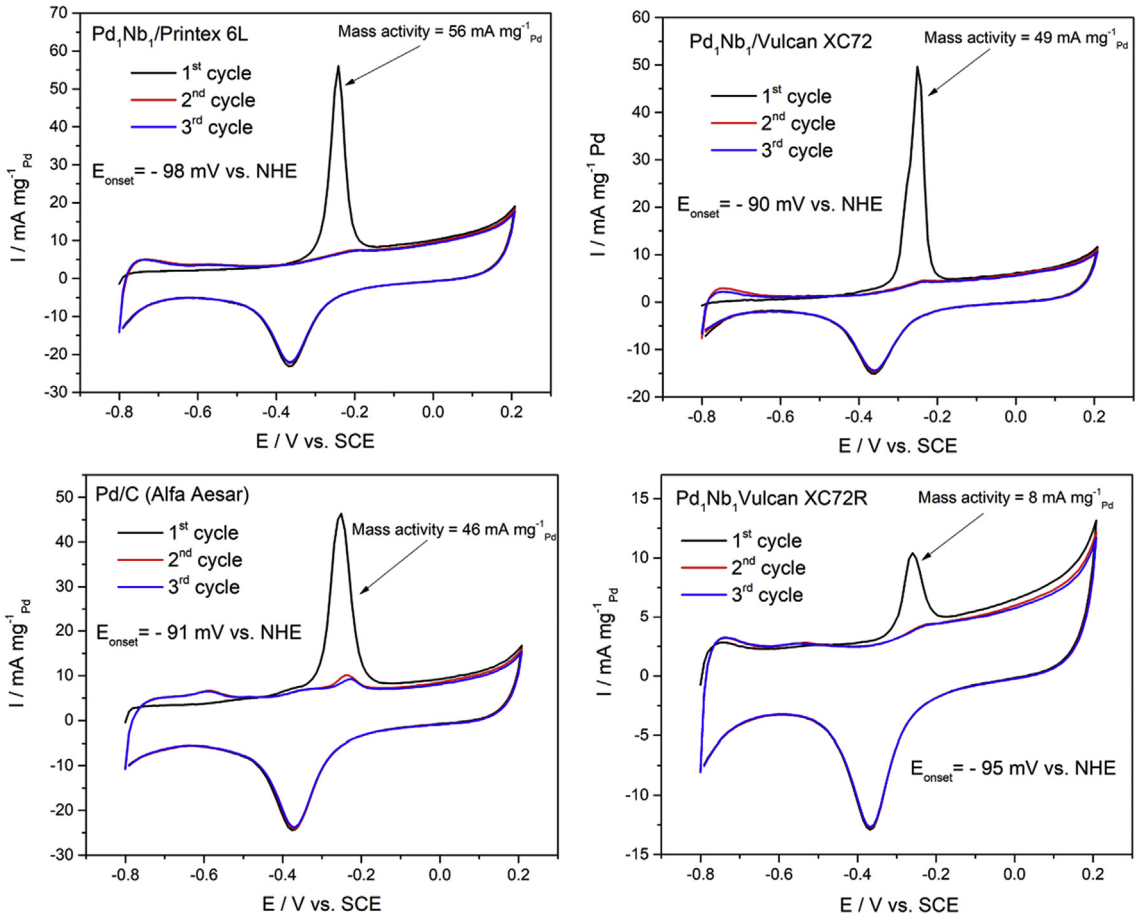

Fig. 10. CO stripping curves of the electrocatalysts in 1 mol L^{-1} KOH at a scan rate of 20 mV s^{-1} at room temperature. Conversion of SCE to NHE by: $E_{NHE} = E_{SCE\ (saturated\ KCl)} + 244$ mV.

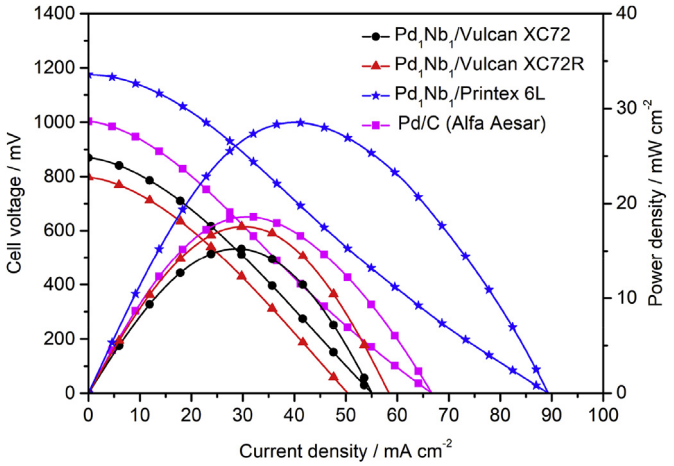

Fig. 11. Polarization and power density curves in the ADEFC. The temperature was set at 70 °C for the fuel cell and 85 °C for the oxygen humidifier. The fuel, 2.0 mol L^{-1} ethanol (in 1.0 mol L^{-1} KOH), was delivered at 1.0 mL min^{-1}, and the oxygen flow was regulated at 200 mL min^{-1}.

addition, this result of 1.17 V vs. NHE of the OCV indicates an excellent energy efficiency of approximately 85%; in contrast, the predicted maximum OCV of the ADEFC calculated previously was 1.38 V vs. NHE, where energy efficiency = *cell voltage real* /*maximum expected cell voltage* $\times$ 100% = 1.17 V/1.38 V $\times$ 100%.

Finally, an experiment was performed to optimize the concentration of ethanol and potassium hydroxide, varying 2, 5 and 7 mol L^{-1} for ethanol and 0.5, 1, 3 and 5 mol L^{-1} for KOH, using a Pd_1Nb_1/Printex 6L electrocatalyst (Fig. 12). According to Fig. 12a, the best performance was 2 mol L^{-1} for ethanol, which shows that increasing the ethanol concentration in the fuel did not increase the power density of the ADEFC. This effect was also observed by Y.S. Li and T.S. Zhao [60] when they increased the ethanol concentration to 5 and 7 mol L^{-1}. According to the authors, high concentrations of ethanol will break the competitive adsorption exchange between ethanol and OH^- ions at the active sites of the anode, thus reducing the electrochemical kinetics of the EOR. In this study, the same effect was evidenced by the decrease in OCV in Fig. 12a. The authors also stated that a concentration of ethanol that are too high will also block the transport of OH^- ions, which leads to an internal resistance increasing.

On the other hand, increasing the KOH concentration to 3 mol L^{-1} of electrolyte improved the maximum power density to 27 mW cm^{-2}, as shown in Fig. 12b. This happens mainly because high pH values increase the EOR electrochemical kinetics, as seen in the OCV shown in Fig. 12b. However, this effect is limited, because 5 mol L^{-1} of KOH decreased the OCV of the cell and consequently decreased the power density of the cell (Fig. 12b). This phenomenon occurs because the excessive concentration of hydroxyl ions not only reduces the coverage of ethanol at the active sites of the anode but also increases the internal resistance, as shown by Y.S. Li and T.S. Zhao [60] and Z. Zhang, L. Xin, and W. Li [61].

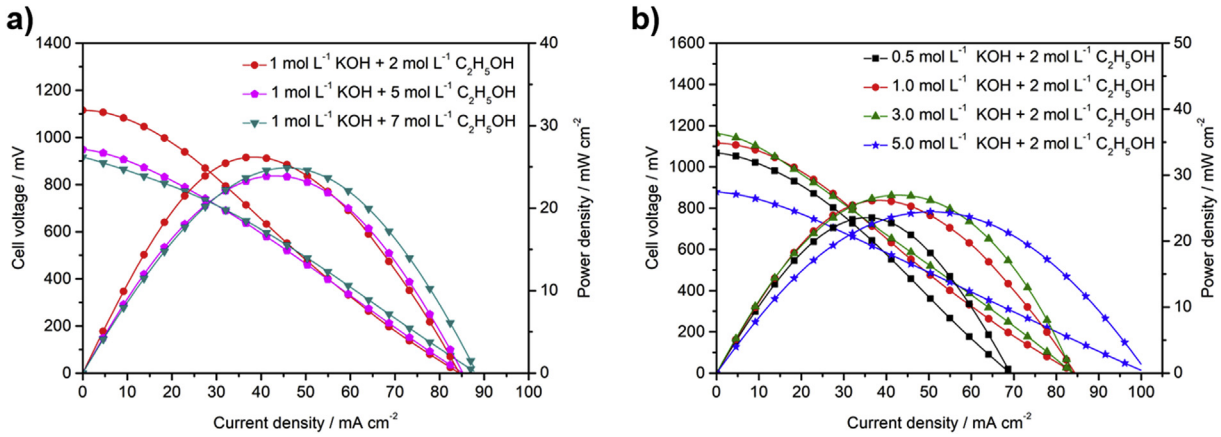

Fig. 12. Polarization and power density curves in the ADEFC under different conditions of ethanol and KOH. The temperature was set at 70 °C for the fuel cell and 85 °C for the oxygen humidifier. The fuel was delivered at 1.0 mL min^{-1}, and the oxygen flow was regulated at 200 mL min^{-1}.

Table 6
ADEFC performance with the open-circuit voltage (OCV) and maximum power density (p_{max}) reported in the literature.

Anode	Cathode	O_2 (mL min^{-1})	Membrane	T (°C)	p_{max} (mW cm^{-2})	OCV (V)	Ref.
Pd_1Nb_1/P	Pt/C (Alfa Aesar)	200	Nafion® 117	70	28	1.17	This work
Pd_9Sn_1/R	Pt/C BASF	150	Fumasep® FAA3	75	15	0.89	[50]
$Pd_4Ni_5Sn_1$/C	Pt/C E-TEK	Large excess	Nafion® 117	100	39	0.86	[51]
Nonplatinum HYPERMEC™	Nonplatinum HYPERMEC™	Large excess	Tokuyama® A201	60	30	0.82	[52]
Pd_9Sn_1/MWCNT	Pd/MWCNT	500	Fumasep® FAA3	85	35	0.78	[53]
Pt/C	PtRu/C	250	KOH-doped PVA/CNT	30	33	0.83	[54]
$PdCeO_2$/C HYPERMEC™	CoFe/C HYPERMEC™	Large excess	KOH-doped Q-PVA/Q-chitosan	60	20	0.70	[55]
Pd/C	CoFe/C HYPERMEC™	100	Tokuyama® A301	80	37	0.83	[56]
Pd_7Ir_3/C	Pt/C BASF	150	Nafion® 117	70	10	0.79	[57]
$Pt_4Ir_1Sn_3$	Pt/C Johnson Matthey	60[a]	Nafion® 117	90	29	0.85	[58]
PtSn/C	Pt/C E-Tek	500[b]	Nafion® 117	100	32	0.77	[59]

P = Printex 6L; R = Vulcan XC72R; C = Vulcan XC72; MWCNT = Multi Wall Carbon Nanotubes (CNT); FWCNT = few-walled CNT; PVA = polyvinyl alcohol; Q = quaternized. All anodes and cathodes have ≥1 mg metal cm^{-2}; all results are for fuel ethanol flow ≥1 mL min^{-1} under [a]1.5 bar or [b] 2 bar of pressure.

We suggest that the results obtained in this study are provided by the contribution of a few factors: 1) the superior hydrophilicity of Printex 6L due to the greater amount of oxygenated groups on its surface [27]; 2) the higher electron transfer rate due to the higher degree of disorder in the hexagonal sp^2 carbon structure related to vacancies in Printex 6L [32]; and 3) it is easier to oxidize CO bound to Pd due to the presence of oxygenated specimens caused by the bifunctional effect of Nb near the electrocatalytic site of Pd [12,13].

5. Conclusions

In CV, Pd_1Nb_1/Printex 6L (50:50 wt%) exhibited 2.2 times higher mass activity than that of the Pd/C (Alfa Aesar); their mass activities were 1300 and 590 mA mg_{Pd}^{-1}, respectively. Moreover, the E_{onset} for EOR was more negative than all the other studied electrocatalysts. The best performance for the ADEFC was obtained using Pd_1Nb_1/Printex 6L, which yielded a maximum power density and open-circuit voltage were 26 mW cm^{-2} and 1.17 V, respectively. The concentration of 2 mol L^{-1} ethanol +3 mol L^{-1} KOH achieved the highest maximum power density, which was 28 mW cm^{-2} for the Pd_1Nb_1/Printex 6L electrocatalyst. We suggest that the higher hydrophilicity and higher degree of disorder of Printex 6L corroborate these results, as shown by the contact angle and Raman spectrum results, respectively. In addition, the electronic and bifunctional effects were evident due to the presence of Nb in the electrocatalysts, as indicated by the Pd crystal expansion by means of the lattice parameter and CO-stripping experiment, respectively. Therefore, it was notable that the support has an essential importance—as good cocatalyst—in the electrocatalytic performance.

Declaration of competing interest

The authors declare no conflict of interest.

Acknowledgments

The authors would like to thank FAPESP (2015/10314–8, 2017/00819–8, 2017/10118-0, 2017/22976–0, 2017/21846–6, and 2017/26288–1), CNPq (406612/2013–7, 429727/2018–6), CAPES, and the use of TEM facilities (JEOL JEM-2100F) of LNNano-CNPEM is greatly acknowledged. Also, the authors are grateful to the Multiuser Central Facilities (UFABC) for the experimental support.

Appendix A. Supplementary data

Supplementary data to this article can be found online at https://doi.org/10.1016/j.renene.2019.12.110.

References

[1] B. McNicol, D.A. Rand, K. Williams, Direct methanol–air fuel cells for road transportation, J. Power Sources 83 (1999) 15–31, https://doi.org/10.1016/S0378-7753(99)00244-X.
[2] T. Yuan, J. Yang, Y. Wang, H. Ding, X. Li, L. Liu, H. Yang, Anodic diffusion layer with graphene-carbon nanotubes composite material for passive direct methanol fuel cell, Electrochim. Acta 147 (2014) 265–270, https://doi.org/

10.1016/j.electacta.2014.09.124.
[3] J.M. Sieben, M.M.E. Duarte, Nanostructured Pt and Pt–Sn catalysts supported on oxidized carbon nanotubes for ethanol and ethylene glycol electro-oxidation, Int. J. Hydrogen Energy 36 (2011) 3313–3321, https://doi.org/10.1016/j.ijhydene.2010.12.020.
[4] V. Bambagioni, C. Bianchini, Y. Chen, J. Filippi, P. Fornasiero, M. Innocenti, A. Lavacchi, A. Marchionni, W. Oberhauser, F. Vizza, Energy efficiency enhancement of ethanol electrooxidation on Pd-CeO2/C in passive and active polymer electrolyte-membrane fuel cells, ChemSusChem 5 (2012) 1266–1273, https://doi.org/10.1002/cssc.201100738.
[5] J.P. Pereira, D.S. Falcão, V.B. Oliveira, A.M.F.R. Pinto, Performance of a passive direct ethanol fuel cell, J. Power Sources 256 (2014) 14–19, https://doi.org/10.1016/j.jpowsour.2013.12.036.
[6] V. Bambagioni, C. Bianchini, A. Marchionni, J. Filippi, F. Vizza, J. Teddy, P. Serp, M. Zhiani, Pd and Pt–Ru anode electrocatalysts supported on multi-walled carbon nanotubes and their use in passive and active direct alcohol fuel cells with an anion-exchange membrane (alcohol=methanol, ethanol, glycerol), J. Power Sources 190 (2009) 241–251, https://doi.org/10.1016/j.jpowsour.2009.01.044.
[7] L. Jiang, A. Hsu, D. Chu, R. Chen, Ethanol electro-oxidation on Pt/C and PtSn/C catalysts in alkaline and acid solutions, Int. J. Hydrogen Energy 35 (2010) 365–372, https://doi.org/10.1016/j.ijhydene.2009.10.058.
[8] S. Beyhan, K. Uosaki, J.M. Feliu, E. Herrero, Electrochemical and in situ FTIR studies of ethanol adsorption and oxidation on gold single crystal electrodes in alkaline media, J. Electroanal. Chem. 707 (2013) 89–94, https://doi.org/10.1016/j.jelechem.2013.08.034.
[9] J. Silva, R. De Souza, M. Romano, PtSnIr/C anode electrocatalysts: promoting effect in direct ethanol fuel cells, J. Braz. Chem. Soc. 23 (6) (2012) 1146–1153, https://doi.org/10.1590/S0103-50532012000600021.
[10] H. Wang, C. Wang, H. Yan, H. Yi, J. Lu, Precisely-controlled synthesis of Au@ Pd core–shell bimetallic catalyst via atomic layer deposition for selective oxidation of benzyl alcohol, J. Catal. 324 (2015) 59–68.
[11] G.M. Alvarenga, I.B.C. Gallo, H.M. Villullas, Enhancement of ethanol oxidation on Pd nanoparticles supported on carbon-antimony tin oxide hybrids unveils the relevance of electronic effects, J. Catal. 348 (2017) 1–8.
[12] F. Moura Souza, L.S. Parreira, P. Hammer, B.L. Batista, M.C. Santos, Niobium: a promising Pd co-electrocatalyst for ethanol electrooxidation reactions, J. Solid State Electrochem. (2017), https://doi.org/10.1007/s10008-017-3802-1.
[13] F.M. Souza, J. Nandenha, B.L. Batista, V.H.A. Oliveira, V.S. Pinheiro, L.S. Parreira, A.O. Neto, M.C. Santos, PdxNbyelectrocatalysts for DEFC in alkaline medium: stability, selectivity and mechanism for EOR, Int. J. Hydrogen Energy (2018), https://doi.org/10.1016/j.ijhydene.2018.01.058.
[14] International Carbon Black Association (ICBA), ICBA, Carbon Black User's Guide, 2004.
[15] C.M. Long, M.A. Nascarella, P.A. Valberg, Carbon black vs. black carbon and other airborne materials containing elemental carbon: physical and chemical distinctions, Environ. Pollut. (2013), https://doi.org/10.1016/j.envpol.2013.06.009.
[16] M. Zahmakıran, S. Özkar, C.A. Mirkin, T.J. Trentler, K.M. Hickman, S.C. Goel, A.M. Viano, P.C. Gibbons, W.E. Buhro, A.M. Morales, C.M. Lieber, W. Pan, Z.R. Dai, Z.L. Wang, T. Haugan, P.N. Barnes, R. Wheeler, F. Meisenkothen, M. Sumption, R. Elghanian, J.J. Storhoff, R.C. Mucic, R.L. Letsinger, C.A. Mirkin, M. Ferrari, P.S. Waggoner, H.G. Craighead, C. Jianronga, M. Yuqing, H. Nongyue, W. Xiaohua, L. Sijiao, A.J. Haes, S. Zou, G.C. Schatz, R.P.V. Duyne, J.N. Anker, W.P. Hall, O. Lyandres, N.C. Shah, J. Zhao, R.P.V. Duyne, B. Sun, E. Marx, N.C. Greenham, M. Law, L.E. Greene, J.C. Johnson, R. Saykally, P. Yang, B.R. Saunders, M.L. Turner, J. Panyam, J. Labhasetwar, D.A. Lavan, T. McGuire, R. Langer, B.E. Rabinow, S.H. Joo, S.J. Choi1, I. Oh, J. Kwak, Z. Liu, O. Terasaki, R. Ryoo, C. Wang, M. Waje, X. Wang, J.M. Tang, R.C. Haddon, Y. Yan, V.L. Colvin, M.C. Schlamp, A.P. Alivisatos, A.L. Rogach, N. Gaponik, J.M. Lupton, C. Bertoni, D.E. Gallardo, S. Dunn, N.L. Pira, M. Paderi, P. Repetto, S.G. Romanov, C.O. Dwyer, C.M.S. Torres, A. Eychmüller, M.T. Reetz, M. Winter, G. Dumpich, J. Lohau, S. Friedrichowski, J.C. Hulteen, D.A. Treichel, M.T. Smith, M.L. Duval, T.R. Jensen, R.P.V. Duyne, F. Hua, J. Shi, Y. Lvov, T. Cui, C.B. Murray, C.R. Kagan, M.G. Bawendi, P. Michler, A. Kiraz, C. Becher, W.V. Schoenfeld, P.M. Petroff, L.D. Zhang, E. Hu, A. Imamoglu, P.M. Petroff, A.C. Gossard, R.A. Logan, W. Wiegmann, S.J. Tans, M.H. Devoret, H.J. Dai, A. Thess, R.E. Smalley, L.J. Geerligs, C. Dekker, H. Yu, J. Li, R.A. Loomis, P.C. Gibbons, L.-W. Wang, W.E. Buhro, M. Antonietti, C. Göltner, J.D. A III, R.G. Finke, D. Astruc, F. Lu, J.R. Aranzaes, R. Narayanan, M.A. El-Sayed, G. Schmid, V. Maihack, F. Lantermann, S. Peschel, A. Doyle, S.K. Shaikhutdinov, S.D. Jackson, H.J. Freund, R. Pool, M. Poliakoff, J.M. Fitzpatrick, T.R. Farren, P.T. Anastas, A. Roucoux, J. Schulz, H. Patin, B.L. Cushing, V.L. Kolesnichenko, C.J. O'Connor, H. Bönneman, R.M. Richards, B.L. Cushing, V.L. Kolesnichenko, C.J. O'Connor, N. Toshima, T. Yonezawa, J. Zhang, J. Worley, S. Denommee, C. Kingston, Z.J. Jakubek, Y. Deslandes, M. Post, B. Simard, N. Braidy, G.A. Botton, M.S. Sibbald, G. Chumanov, T.M. Cotton, M.-S. Yeh, Y.-S. Yang, Y.-P. Lee, H.-F. Lee, Y.-H. Yeh, C.-S. Yeh, Y. Lin, R.G. Finke, C. Pan, K. Pelzer, K. Philippot, B. Chaudret, F. Dassenoy, P. Lecante, M.-J. Casanove, J. Yang, T.C. Deivaraj, H.P. Too, J.Y. Lee, M. Zahmakiran, S. Özkar, M. Zahmakiran, S. Özkar, N. Zheng, J. Fan, G.D. Stucky, M. Zahmakiran, S. Özkar, Y. Hou, J. Yua, S. Gao, K.-C. Huang, S.H. Ehrman, Y. Sun, Y. Xia, H. Hirai, Y. Nakao, N. Toshima, H. Cui, M. Zayat, D. Levy, C.-C. Wang, J.Y. Ying, M.T. Reetz, W. Helbig, M.T. Reetz, G. Lohmer, K.S. Suslick, S.-B. Choe, A.A. Cichowias, M.W. Grinstaff, N.A. Dhas, K.S. Suslick, M.J. Meziani, H.W. Rollins, L.F. Allard, Y.-P. Sun, H. Lee, S.E. Habas, S. Kweskin, D. Butcher, G.A. Somorjai, P. Yang, N. Toshima, M. Harada, Y. Yamazaki, K. Asakura, N. Toshima, T. Takahashi, G.A. Somorjai, H. Frei, J.Y. Park, R. Narayanan, M.A. El-Sayed, A.R. Tao, S. Habas, P.D. Yang, S. Özkar, R.G. Finke, L.S. Ott, R.G. Finke, B.W. Ninham, E. Bayram, M. Zahmakiran, S. Özkar, R.G. Finke, S. Özkar, R.G. Finke, S. Özkar, R.G. Finke, M. Zahmakiran, S. Özkar, T. Kodaira, T. Shiomi, R. Narayanan, M.A. El-Sayed, I. Pastoriza-Santos, L.M. Liz-Marzan, M. Zhao, L. Sun, R.M. Crooks, L. Balogh, D.A. Tomalia, G. Schmid, B. Morun, J.O. Malm, F. Dassenoy, K. Philippot, T.O. Ely, C. Amiens, P. Lecante, E. Snoeck, A. Mosset, M.J. Casanove, B. Chaudret, J. Yang, J.Y. Lee, T.C. Deivaraj, H.-P. Too, W.W. Weare, S.M. Reed, M.G. Warner, J.E. Hutchison, S.U. Son, Y. Jang, K.Y. Yoon, E. Kang, T. Hyeon, K. Pelzer, B. Laleu, F. Lefebvre, K. Philippot, B. Chaudret, J.P. Candy, J.M. Basset, M. Zahmakiran, M. Tristany, K. Philippot, K. Fajerwerg, S. Özkar, B. Chaudret, B.J. Hornstein, R.G. Finke, F. Durap, M. Zahmakiran, S. Özkar, F. Durap, M. Zahmakiran, S. Özkar, S. Özkar, R.G. Finke, L. Tosheva, V.P. Valtchev, H. Kato, T. Minami, T. Kanazawa, Y. Sasaki, E. Castillejos, P.J. Debouttiere, L. Roiban, A. Solhy, V. Martinez, Y. Kihn, O. Ersen, K. Philippot, B. Chaudret, P. Serp, D.C. Sayle, J.A. Doig, S.C. Parker, G.W. Watson, M. Haruta, F. Shi, Q. Zhang, Y. Ma, Y. He, Y. Deng, M. Graeser, E. Pippel, A. Greiner, J.H. Wendorff, K. Kaneda, T. Mizugaki, M. Zahmakiran, Y. Tonbul, S. Özkar, M.S. El-Shall, V. Abdelsayed, A.E.R.S. Khder, H.M.A. Hassan, H.M. El-Kaderi, T.E. Reich, Z. Peng, J. Wu, H. Yang, V. Mazumder, S.H. Sun, M. Zahmakiran, S. Özkar, M. Zahmakiran, S. Özkar, F. Su, L. Lv, F.Y. Lee, T. Liu, A.I. Cooper, X.S. Zhao, H. Kato, T. Minami, T. Kanazawa, Y. Sasaki, H. Choi, S.R. Al-Abed, S. Agarwal, D.D. Dionysiou, A. Barau, V. Budarin, A. Caragheorgheopol, R. Luque, D.J. Macquarrie, A. Prelle, V.S. Teodorescu, M. Zaharescu, M. Haruta, S. Tsubota, T. Kobayashi, T. Kageyama, M.J. Genet, A. Martinez, G. Prieto, P. He, M. Zhang, D. Yang, J. Yang, S. Dominguez-Dominguez, J. Arias-Pardilla, A. Berenguer-Murcia, E. Morallon, D. Cazorla-Amoros, N. Panziera, P. Pertici, L. Barazzone, A.M. Caporusso, G. Vitulli, P. Salvadori, S. Borsacchi, M. Geppi, C.A. Veracini, G. Martra, L. Bertinetti, S.M. George, X. Jiang, H. Huang, F.B. Prinz, S.F. Bent, H. Feng, J.W. Elam, J.A. Libera, W. Setthapun, P.C. Stair, I.J. Hsu, D.A. Hansgen, B.E. McCandless, B.G. Willis, J.G. Chen, A.S.C. Chan, J.J. Pluth, J. Halpern, R.H. Crabtree, M.F. Mellea, J.M. Mihelcic, J.M. Quirk, J. Schwartz, J.A. Widegren, R.G. Finke, R.A. Sheldon, A.J. Bard, M.A. Fox, X. Chen, S. Shen, L. Guo, S.S. Mao, T. Torimoto, T. Adachi, K. Okazaki, M. Sakuraoka, T. Shibayama, B. Ohtani, A. Kudo, S. Kuwabata, G.N. Schrauzer, T.D. Guth, J. Zhang, Q. Xu, Z. Feng, M. Li, C. Li, D. Duonghong, E. Borgarello, M. Gratzel, K. Maeda, K. Teramura, N. Saito, Y. Inoue, K. Domen, J. Sato, N. Saito, Y. Yamada, K. Maeda, T. Tsuyoshi, J.N. Kondo, M. Hara, H. Kobayashi, K. Domen, Y. Inoue, K. Teramura, K. Maeda, T. Saito, T. Takata, N. Saito, Y. Inoue, K. Domen, K. Maeda, K. Teramura, D. Lu, N. Saito, Y. Inoue, K. Domen, K. Maeda, K. Teramura, D. Lu, N. Saito, Y. Inoue, K. Domen, K. Maeda, K. Teramura, D. Lu, K. Domen, S. Shen, L. Guo, S. Shen, L. Guo, P.V. Kamat, S. Chuangchote, J. Jitputti, T. Sagawa, S. Yoshikawa, J. Jitputti, Y. Suzuki, S. Yoshikawa, S.C. Amendola, J.M. Janjua, N.C. Spencer, M.T. Kelly, P.J. Petillo, S.L. Sharp-Goldman, M. Binder, M. Chandra, Q. Xu, U.B. Demirci, P. Miele, C.W. Hamilton, R.T. Baker, A. Staubitz, I. Manners, Ö. Metin, S. Özkar, N. Patel, G. Guella, A. Kale, A. Miotello, B. Patton, C. Zanchetta, L. Mirenghi, P. Rotolo, Ö. Metin, S. Özkar, Ö. Metin, S. Özkar, A. Garron, D. Świerczyński, S. Bennici, A. Auroux, X. Yang, F. Cheng, J. Liang, Z. Tao, J. Chen, Z. Liu, B. Guo, S.H. Chan, E.H. Tang, L. Hong, Y. Liang, H.-B. Dai, L.-P. Ma, P. Wang, H.-M. Cheng, M. Zahmakiran, S. Özkar, M. Zahmakiran, S. Özkar, M. Rakap, S. Özkar, M. Zahmakiran, T. Ayvalı, S. Akbayrak, S. Çalışkan, D. Çelik, S. Özkar, Q. Xu, M. Chandra, Q. Xu, M. Chandra, T. Umegaki, J.-M. Yan, X.-B. Zhang, H. Shioyama, N. Kuriyama, Q. Xu, F. Cheng, H. Ma, Y. Li, J. Chen, J.-M. Yan, X.-B. Zhang, S. Han, H. Shioyama, Q. Xu, S.B. Kalidindi, U. Sanyal, B.R. Jagirdar, T. Umegaki, J.-M. Yan, X.-B. Zhang, H. Shioyama, N. Kuriyama, Q. Xu, J.-M. Yan, X.-B. Zhang, S. Han, H. Shioyama, Q. Xu, M. Zahmakıran, F. Durap, S. Özkar, Ö. Metin, V. Mazumder, S. Özkar, S. Sun, T. Umegaki, J.-M. Yan, X.-B. Zhang, H. Shioyama, N. Kuriyama, Q. Xu, M. Chandra, Q. Xu, M. Chandra, Q. Xu, M. Zahmakıran, S. Özkar, T.J. Clark, G.R. Whittell, I. Manners, Ö. Metin, Ş. Şahin, S. Özkar, J.-M. Yan, X.-B. Zhang, S. Han, H. Shioyama, Q. Xu, J.-M. Yan, X.-B. Zhang, T. Akita, M. Haruta, Q. Xu, X. Yang, F. Cheng, Z. Tao, J. Chen, K. Kurihara, J.H. Fendler, I. Ravet, J.B. Nagy, J.D. A III, R.G. Finke, J.D. A III, R.G. Finke, Y.Y. Hong, A. Sen, S. Ikeda, S. Ishino, T. Harada, N. Okamoto, T. Sakata, H. Mori, S. Kuwabata, T. Torimoto, M. Matsumura, M. Adlim, M. Abu-Bakar, K.Y. Liew, J. Ismail, L. Wu, B.-L. Li, Y.-Y. Huang, H.-F. Zhou, Y.-M. He, Q.-H. Fan, T. Mizugaki, M. Murata, S. Fukubayashi, T. Mitsudome, K. Jitsukawa, K. Kaneda, L. Wu, B.-L. Li, Y.-Y. Huang, H.-F. Zhou, Y.-M. He, Q.-H. Fan, S. Ikeda, S. Ishino, T. Harada, N. Okamoto, T. Sakata, H. Mori, S. Kuwabata, T. Torimoto, M. Matsumura, J.E. Mondloch, X. Yan, R.G. Finke, J.A. Widegren, R.G. Finke, M. Zahmakiran, T. Kodaira, S. Özkar, I.S. Park, M.S. Kwon, N. Kim, J.S. Lee, K.Y. Kang, J. Park, M. Zahmakiran, Y. Tonbul, S. Özkar, B. Yoon, H.-B. Pan, C.M. Wai, H.-B. Pan, C.M. Wai, H.-B. Pan, C.M. Wai, J. Pellegatta, C. Blandy, V. Colliere, R. Choukroun, B. Chaudret, P. Cheng, K. Philippot, B. Yoon, C.M. Wai, H. Dai, V. Georgakilas, D. Gournis, V. Tzitzios, L. Pasquato, D.M. Guldie, M. Prato, X. Pan, Z. Fan, W. Chen, Y. Ding, H. Luo, X. Bao, M. Kidwai, S. Saxena, R. Mohan, R. Venkataramanan, A. Spitaleri, P. Pertici, N. Scalera, G. Vitulli, M. Hoang, T.W. Turney, M. Gleria, A. Drelinkiewiczaa, A. Waksmundzkaa, W. Makowskia, J.W. Sobczakb, A. Krola, A. Zieba, P. Concepcion, A. Corma, J. Silvestre-Albero, V. Franco, J.Y. Chane-Ching, S. Özkar, R.G. Finke, M. Kidwaia, N.K. Mishraa, V. Bansala, A. Kumarb, S. Mozumdarb, N. Miyaura, A. Suzuki, J. Hassan, M. SRvignon, C. Gozzi, E. Schulz, M. Lemaire, D. Astruc, S. Mandal, D. Roy, R.V. Chaudhari, M. Sastry, M. Moreno-Manas, R. Pleixats, S. Villarroya, M.A.R. Meier, M. Filali, J.-F. Gohy,

U.S. Schubert, J. Zhu, J. Zhou, T. Zhao, X. Zhou, D. Chen, W. Yuan, B. Baruwati, D. Guin, S.V. Manorama, W. Han, C. Liu, Z. Jina, V. Chandrasekhar, R.S. Narayanan, P. Thilagar, M.T. Reetz, E. Westermann, R. Tatumi, T. Akita, H. Fujihara, V. Kogan, Z. Aizenshtat, R. Popovitz-Biro, R. Neumann, C.P. Mehnert, D.W. Weaver, J.Y. Ying, K. Mori, K. Yamaguchi, T. Hara, T. Mizugaki, K. Ebitani, K. Kaneda, J. Schwarz, V.P.W. Bohm, M.G. Gardiner, M. Grosche, W.A. Herrmann, W. Hieringer, G. Raudaschl-Sieber, K. Koehler, R.G. Heidenreich, J.G.E. Krauter, J. Pietsch, L. Djakovitch, K. Koehler, J. Park, E. Kang, S.U. Son, H.M. Park, M.K. Lee, J. Kim, K.W. Kim, H.-J. Noh, J.-H. Park, C.J. Bae, J.-G. Park, T. Hyeon, V.K. Kanuru, S.M. Humphrey, J.M.W. Kyffin, D.A. Jefferson, J.W. Burton, M. Armbrüster, R.M. Lambert, S.K. Beaumont, G. Kyriakou, R.M. Lambert, U. Son, Y. Jang, J. Park, H.B. Na, H.M. Park, H.J. Yun, J. Lee, T. Hyeon, B. Cornils, E.G. Kuntz, C. Larpent, H. Patin, C. Larpent, E. Bernard, F.B.-L. Menn, H. Patin, A. Walther, A.H.E. Müller, N. Glaser, J.A. Dave, A. Boker, G. Krausch, B.P. Binks, J.A. Rodrigues, J. Faria, M.P. Ruiz, D.E. Resascoa, M. Zhao, R.M. Crooks, Y. Niu, L.K. Yeung, R.M. Crooks, R.M. Crooks, M. Zhao, L. Sun, V. Chechik, L.K. Yeung, M. Ooe, M. Murata, T. Mizugaki, K. Ebitani, K. Kaneda, S. Kidambi, J. Dai, J. Li, M.L. Bruening, K. Li, Y. Wang, J. Jiang, Z. Jin, J. Schulz, A. Roucoux, H. Patin, J. Schulz, A. Roucoux, H. Patin, J. Schulz, A. Roucoux, E. Ramirez, K. Philippot, B. Chaudret, V. Mevellec, C. Mattioda, J. Schulz, J.P. Rolland, A. Roucoux, A. Nowicki, Y. Zhang, B. Leger, J.P. Rolland, H. Bricout, E. Monflier, A. Roucoux, M.V. Vasylyev, G. Maayan, Y. Hovav, A. Haimov, R. Neumann, A. Denicourt-Nowicki, A. Ponchel, E. Monflier, A. Roucoux, V. Mevellec, A. Nowicki, A. Roucoux, C. Dujardin, P. Granger, E. Payen, K. Philippot, M. Boutros, F. Launay, A. Nowicki, T. Onfroy, V. Herledan-Semmer, A. Roucoux, A. Gedeon, C. Hubert, A. Denicourt-Nowicki, P. Beaunier, A. Roucoux, L. Song, X. Li, H. Wang, H. Wu, P. Wu, N.M. Callis, E. Thiery, J.L. Bras, J. Muzart, S.-J. Chiang, B.-J. Liaw, Y.-Z. Chen, K. Yoshida, C. Gonzalez-Arellanob, R. Luquec, P.L. Gaia, E.H. Rahim, F.S. Kamounah, J. Frederiksen, J.B. Christensen, S. Proch, Y. Mei, J.M.R. Villanueva, Y. Lu, A. Karpov, M. Ballauff, R. Kempea, S. Sawoo, D. Srimani, P. Dutta, R. Lahiri, A. Sarkar, A. Ohtaka, Y. Tamaki, Y. Igawa, K. Egami, O. Shimomura, R. Nomura, Y. Li, X.M. Hong, D.M. Collard, M.A. El-Sayed, Y. Li, M.A. El-Sayed, R. Narayanan, M.A. El-Sayed, L. Strimbu, J. Liu, A.E. Kaifer, G.M. Scheuermann, L. Rumi, P. Steurer, W. Bannwarth, R. Mulhaupt, F. Durap, M. Rakap, M. Aydemir, S. Özkar, J. Han, Y. Liu, R. Guo, Y. Li, X. Fan, J. Qi, J. Ji, S. Wang, G. Zhang, F. Zhang, P. Venkatesan, J. Santhanalakshmi, J. Dupont, R.F. de Souza, P.A.Z. Suarez, V.I. Parvulescu, C. Hardacre, C.W. Scheeren, G. Machado, J. Dupont, P.F.P. Fichtner, S.R. Texeira, J. Dupont, G.S. Fonseca, A.P. Umpierre, P. Fichtner, S.R. Teixeira, G.S. Fonseca, A.P. Umpierre, P.F.P. Fichtner, S.R. Teixeira, J. Dupont, J. Huang, T. Jiang, B. Han, H. Gao, Y. Chang, G. Zhao, W. Wu, B. Leger, A. Denicourt-Nowicki, A. Roucoux, H. Olivier-Bourbigou, X. Yang, N. Yan, Z. Fei, R.M. Crespo-Quesada, G. Laurenczy, L. Kiwi-Minsker, Y. Kou, Y. Li, P.J. Dyson, X.-D. Mu, D.G. Evans, Y. Kou, X.-D. Mu, J.-Q. Meng, Z.-C. Li, Y. Kou, V. Mevellec, B. Leger, M. Mauduit, A. Roucoux, J. Huang, T. Jiang, H. Gao, B. Han, Z. Liu, W. Wu, Y. Chang, G. Zhao, B. Hu, T. Wu, K. Ding, X.i. Zhou, T. Jiang, B. Han, S. Miao, Z. Liu, B. Han, J. Huang, Z. Sun, J. Zhang, T. Jiang, S. Miao, Z. Liu, B. Han, J. Huang, Z. Sun, J. Zhang, T. Jiang, C.C. Cassol, A.P. Umpierre, G. Machado, S.I. Wolke, J. Dupont, X. Yang, Z. Fei, D. Zhao, W.H. Ang, Y. Li, P.J. Dyson, N.A. Hamill, C. Hardacre, S.E. McMath, R.R. Deshmukh, R. Rajagopal, K.V. Srinivasan, V. Caló, A. Nacci, A. Monopoli, S. Laera, N. Cioffi, V. Caló, A. Nacci, A. Monopoli, A. Detomaso, P. Iliade, V. Calo, A. Nacci, A. Monopoli, F. Montingelli, A.R. Gholap, K. Venkatesan, R. Pasricha, T. Daniel, R.J. Lahoti, K.V. Srinivasan, B. Lindstrom, L.J. Pettersson, M. Poliakoff, J.M. Fitzpatrick, T.R. Farren, P.T. Anastas, J.M. Campelo, T.D. Conesa, M.J. Gracia, M.J. Jurado, R. Luque, J. Marinas, A.A. Romero, V. Budarin, J.H. Clark, R. Luque, D.J. Macquarrie, R.J. White, Z. Zhang, Z. Wang, C.O. Kappe, J.E. Mondloch, Q. Wang, A.I. Frenkel, R.G. Finke, J.E. Mondloch, X. Yan, R.G. Finke, J.C. Park, J.U. Bang, J. Lee, C.H. Ko, H. Song, Y. Lu, Y. Zin, Z.Y. Li, Y. Xia, J.Y. Kim, S.B. Yoon, J.-S. Yu, M. Kim, K. Sohn, H.B. Na, T. Hyeon, Y.L. Shi, T. Asefa, Metal nanoparticles in liquid phase catalysis; from recent advances to future goals, Nanoscale 3 (2011) 3462, https://doi.org/10.1039/c1nr10201j.

[17] E.D. Kuempel, T. Sorahan, Carbon black, J Cancer Appl Occup Env. Hyg Am J Public Heal. (2009), https://doi.org/10.1007/SpringerReference_208034.

[18] A.K. Sahu, K.G. Nishanth, G. Selvarani, P. Sridhar, S. Pitchumani, A.K. Shukla, Polymer electrolyte fuel cells employing electrodes with gas-diffusion layers of mesoporous carbon derived from a sol-gel route, Carbon N. Y. (2009), https://doi.org/10.1016/j.carbon.2008.09.031.

[19] W. Han, W. Zhu, P. Zhang, Y. Zhang, L. Li, Photocatalytic degradation of phenols in aqueous solution under irradiation of 254 and 185 nm UV light, Catal. Today (2004), https://doi.org/10.1016/j.cattod.2004.04.041.

[20] A. Basch, R. Horn, J.O. Besenhard, Substrate induced coagulation (SIC) of nanodisperse carbon black in non-aqueous media: the dispersibility and stability of carbon black in N-methyl-2-pyrrolidinone, Colloids Surfaces A Physicochem. Eng. Asp. (2005), https://doi.org/10.1016/j.colsurfa.2004.09.026.

[21] D. Mirabile Gattia, M.V. Antisari, L. Giorgi, R. Marazzi, E. Piscopiello, A. Montone, S. Bellitto, S. Licoccia, E. Traversa, Study of different nanostructured carbon supports for fuel cell catalysts, J. Power Sources (2009), https://doi.org/10.1016/j.jpowsour.2009.04.058.

[22] A. Brouzgou, A. Podias, P. Tsiakaras, PEMFCs and AEMFCs directly fed with ethanol: a current status comparative review, J. Appl. Electrochem. 43 (2013) 119–136, https://doi.org/10.1007/s10800-012-0513-2.

[23] H.B. Suffredini, et al., Sol–gel method to prepare active Pt–RuO2 coatings on carbon powder for methanol oxidation, Electrochem. Commun. 6 (10) (2004) 1025–1028.

[24] W.R.P. Barros, Q.L. Wei, G.X. Zhang, S.H. Sun, M.R. V Lanza, A.C. Tavares, Oxygen reduction to hydrogen peroxide on Fe3O4 nanoparticles supported on Printex carbon and Graphene, Electrochim. Acta (2015), https://doi.org/10.1016/j.electacta.2015.02.175.

[25] A. Galarneau, D. Mehlhorn, F. Guenneau, B. Coasne, F. Villemot, D. Minoux, C. Aquino, J.P. Dath, Specific surface area determination for microporous/mesoporous materials: the case of mesoporous FAU-Y zeolites, Langmuir (2018), https://doi.org/10.1021/acs.langmuir.8b02144.

[26] M.H.M.T. Assumpção, a. Moraes, R.F.B. De Souza, I. Gaubeur, R.T.S. Oliveira, V.S. Antonin, G.R.P. Malpass, R.S. Rocha, M.L. Calegaro, M.R.V. Lanza, M.C. Santos, Low content cerium oxide nanoparticles on carbon for hydrogen peroxide electrosynthesis, Appl. Catal. Gen. (2012) 411–412, https://doi.org/10.1016/j.apcata.2011.09.030, 1–6.

[27] M.H.M.T. Assumpção, R.F.B. De Souza, D.C. Rascio, J.C.M. Silva, M.L. Calegaro, I. Gaubeur, T.R.L.C. Paixão, P. Hammer, M.R. V Lanza, M.C. Santos, A comparative study of the electrogeneration of hydrogen peroxide using Vulcan and Printex carbon supports, Carbon N. Y. 49 (2011) 2842–2851, https://doi.org/10.1016/j.carbon.2011.03.014.

[28] A. Jorio, L.G. Cançado, Perspectives on Raman spectroscopy of graphene-based systems: from the perfect two-dimensional surface to charcoal, Phys. Chem. Chem. Phys. 14 (2012) 15246, https://doi.org/10.1039/c2cp42621h.

[29] L. Castanheira, L. Dubau, M. Mermoux, G. Berthomé, N. Caqué, E. Rossinot, M. Chatenet, F. Maillard, Carbon corrosion in proton-exchange membrane fuel cells: from model experiments to real-life operation in membrane electrode assemblies, ACS Catal. 4 (2014) 2258–2267, https://doi.org/10.1021/cs500449q.

[30] T.C.S. Evangelista, G.T. Paganoto, M.C.C. Guimarães, J. Ribeiro, Raman spectroscopy and electrochemical investigations of pt electrocatalyst supported on carbon prepared through plasma pyrolysis of natural gas, J. Spectrosc. 2015 (2015), https://doi.org/10.1155/2015/329730.

[31] S.G. da Silva, M.H.M.T. Assumpção, R.F.B. de Souza, G.S. Buzzo, E.V. Spinacé, A.O. Neto, J.C.M. Silva, Electrochemical and fuel cell evaluation of PtIr/C electrocatalysts for ethanol electrooxidation in alkaline medium, Electrocatalysis 5 (2014) 438–444, https://doi.org/10.1007/s12678-014-0213-2.

[32] M. Pawlyta, J.-N. Rouzaud, S. Duber, Raman microspectroscopy characterization of carbon blacks: spectral analysis and structural information, Carbon N. Y. 84 (2015) 479–490, https://doi.org/10.1016/j.carbon.2014.12.030.

[33] Y. Holade, C. Morais, K. Servat, T.W. Napporn, K.B. Kokoh, Enhancing the available specific surface area of carbon supports to boost the electroactivity of nanostructured Pt catalysts, Phys. Chem. Chem. Phys. (2014), https://doi.org/10.1039/c4cp03851g.

[34] A.G. Pandolfo, A.F. Hollenkamp, Carbon properties and their role in supercapacitors, J. Power Sources (2006), https://doi.org/10.1016/j.jpowsour.2006.02.065.

[35] D. Pantea, H. Darmstadt, S. Kaliaguine, C. Roy, Electrical conductivity of conductive carbon blacks: influence of surface chemistry and topology, Appl. Surf. Sci. (2003), https://doi.org/10.1016/S0169-4332(03)00550-6.

[36] X. Wang, H. Zhang, J. Zhang, H. Xu, X. Zhu, J. Chen, B. Yi, A bi-functional microporous layer with composite carbon black for PEM fuel cells, J. Power Sources (2006), https://doi.org/10.1016/j.jpowsour.2006.06.064.

[37] D. Schebarchov, S.C. Hendy, Solid-liquid phase coexistence and structural transitions in palladium clusters, Phys. Rev. B Condens. Matter Mater. Phys. (2006), https://doi.org/10.1103/PhysRevB.73.121402.

[38] T. Pillo, R. Zimmermann, P. Steiner, S. Hüfner, The electronic structure of PdO found by photoemission (UPS and XPS) and inverse photoemission (BIS), J. Phys. Condens. Matter (1997), https://doi.org/10.1088/0953-8984/9/19/018.

[39] S. Li, Q. Xu, E. Uchaker, X. Cao, G. Cao, Comparison of Amorphous, Pseudohexagonal and Orthorhombic Nb2O5 for High-Rate Lithium Ion Insertion, CrystEngComm (2016), https://doi.org/10.1039/c5ce02069g.

[40] E.C.P. Felipe M. Souza, Paula Böhnstedt, Victor S. Pinheiro, M.C. S, Luanna S. Parreira, Bruno L. Batista, Niobium enhances electrocatalytic Pd activity in alkaline direct glycerol fuel cells, ChemElectroChem 6 (2019) 1–12, https://doi.org/10.1002/celc.201901254.

[41] M. Duta, L. Predoana, J.M. Calderon-Moreno, S. Preda, M. Anastasescu, A. Marin, I. Dascalu, P. Chesler, C. Hornoiu, M. Zaharescu, P. Osiceanu, M. Gartner, Nb-doped TiO2 sol-gel films for CO sensing applications, Mater. Sci. Semicond. Process. (2016), https://doi.org/10.1016/j.mssp.2015.11.004.

[42] V.S. Pinheiro, E.C. Paz, L.R. Aveiro, L.S. Parreira, F.M. Souza, P.H.C. Camargo, M.C. Santos, Ceria high aspect ratio nanostructures supported on carbon for hydrogen peroxide electrogeneration, Electrochim. Acta 259 (2018) 865–872, https://doi.org/10.1016/j.electacta.2017.11.010.

[43] L.S. Parreira, J.C.M. da Silva, M. D'Villa -Silva, F.C. Simões, S. Garcia, I. Gaubeur, M.A.L. Cordeiro, E.R. Leite, M.C. dos Santos, PtSnNi/C nanoparticle electrocatalysts for the ethanol oxidation reaction: Ni stability study, Electrochim. Acta 96 (2013) 243–252, https://doi.org/10.1016/j.electacta.2013.02.054.

[44] F.M. Souza, J. Nandenha, B.L. Batista, V.H.A. Oliveira, V.S. Pinheiro, L.S. Parreira, A.O. Neto, M.C. Santos, PdxNbyelectrocatalysts for DEFC in alkaline medium: stability, selectivity and mechanism for EOR, Int. J. Hydrogen Energy 43 (2018) 4505–4516, https://doi.org/10.1016/j.ijhydene.2018.01.058.

[45] S.T. Nguyen, Y. Yang, X. Wang, Ethanol electro-oxidation activity of Nb-doped-TiO2 supported PdAg catalysts in alkaline media, Appl. Catal. B Environ. 113–114 (2012) 261–270, https://doi.org/10.1016/j.apcatb.2011.11.046.

[46] Z.X. Liang, et al., Mechanism study of the ethanol oxidation reaction on palladium in alkaline media, Electrochim. Acta 54 (8) (2009) 2203–2208.

[47] Z. Zhang, L. Xin, K. Sun, W. Li, Pd-Ni electrocatalysts for efficient ethanol oxidation reaction in alkaline electrolyte, Int. J. Hydrogen Energy 36 (2011) 12686–12697, https://doi.org/10.1016/j.ijhydene.2011.06.141.
[48] Y. Ji, et al., Palladium networks decorated by cuprous oxide for remarkably enhanced electrocatalytic activity of methanol oxidation reaction with high CO-tolerance, J. Power Sources 329 (2016) 115–122.
[49] P. Hernández-Fernández, S. Rojas, P. Ocón, J.L.G. de la Fuente, P. Terreros, M.A. Peña, J.L. García-Fierro, An opening route to the design of cathode materials for fuel cells based on PtCo nanoparticles, Appl. Catal. B Environ. 77 (2007) 19–28, https://doi.org/10.1016/j.apcatb.2007.07.002.
[50] PdSn/C electrocatalysts with different atomic ratios for ethanol electro-oxidation in alkaline media, Int. J. Electrochem. 9 (2014) 5416–5424. http://www.electrochemsci.org/papers/vol9/91005416.pdf. accessed June 29, 2017.
[51] L.P.R. Moraes, B.R. Matos, C. Radtke, E.I. Santiago, F.C. Fonseca, S.C. Amico, C.F. Malfatti, Synthesis and performance of palladium-based electrocatalysts in alkaline direct ethanol fuel cell, Int. J. Hydrogen Energy 41 (2016) 6457–6468, https://doi.org/10.1016/j.ijhydene.2016.02.150.
[52] Y.S. Li, T.S. Zhao, Z.X. Liang, Performance of alkaline electrolyte-membrane-based direct ethanol fuel cells, J. Power Sources 187 (2009) 387–392, https://doi.org/10.1016/J.JPOWSOUR.2008.10.132.
[53] A.N. Geraldes, D. Furtunato da Silva, J.C. Martins da Silva, O. Antonio de Sá, E.V. Spinacé, A.O. Neto, M. Coelho dos Santos, Palladium and palladium–tin supported on multi wall carbon nanotubes or carbon for alkaline direct ethanol fuel cell, J. Power Sources 275 (2015) 189–199, https://doi.org/10.1016/j.jpowsour.2014.11.024.
[54] C.Y. Huang, J.S. Lin, W.H. Pan, C.M. Shih, Y.L. Liu, S.J. Lue, Alkaline direct ethanol fuel cell performance using alkali-impregnated polyvinyl alcohol/functionalized carbon nano-tube solid electrolytes, J. Power Sources (2016), https://doi.org/10.1016/j.jpowsour.2015.10.108.
[55] G.M. Liao, C.C. Yang, C.C. Hu, Y.L. Pai, S.J. Lue, Novel quaternized polyvinyl alcohol/quaternized chitosan nano-composite as an effective hydroxide-conducting electrolyte, J. Membr. Sci. (2015), https://doi.org/10.1016/j.memsci.2015.02.043.
[56] L. Zeng, T.S. Zhao, Y.S. Li, Synthesis and characterization of crosslinked poly (vinyl alcohol)/layered double hydroxide composite polymer membranes for alkaline direct ethanol fuel cells, Int. J. Hydrogen Energy 37 (2012) 18425–18432, https://doi.org/10.1016/J.IJHYDENE.2012.09.089.
[57] A.O. Neto, S.G. da Silva, G.S. Buzzo, R.F.B. de Souza, M.H.M.T. Assumpção, E.V. Spinacé, J.C.M. Silva, Ethanol electrooxidation on PdIr/C electrocatalysts in alkaline media: electrochemical and fuel cell studies, Ionics 21 (2015) 487–495, https://doi.org/10.1007/s11581-014-1201-5.
[58] J. Tayal, B. Rawat, S. Basu, Bi-metallic and tri-metallic Pt–Sn/C, Pt–Ir/C, Pt–Ir–Sn/C catalysts for electro-oxidation of ethanol in direct ethanol fuel cell, Int. J. Hydrogen Energy 36 (2011) 14884–14897, https://doi.org/10.1016/j.ijhydene.2011.03.035.
[59] R.F. De Souza, J.C.M. Da Silva, L.S. Parreira, M. DVilla-Silva, F.C. Simões, M.L. Calegaro, M.J. De Giz, G.A. Câmara, A.O. Neto, M.C. Santos, PtSnCe/C and PtSnIr/C Electrocatalysts for Ethanol Oxidation: DEFC and in Situ FTIR Studies, 2011, pp. 1293–1298, https://doi.org/10.1149/1.3635660.
[60] Y.S. Li, T.S. Zhao, A passive anion-exchange membrane direct ethanol fuel cell stack and its applications, Int. J. Hydrogen Energy (2016), https://doi.org/10.1016/j.ijhydene.2016.08.180.
[61] Z. Zhang, L. Xin, W. Li, Electrocatalytic oxidation of glycerol on Pt/C in anion-exchange membrane fuel cell: cogeneration of electricity and valuable chemicals, Appl. Catal. B Environ. 119–120 (2012) 40–48, https://doi.org/10.1016/j.apcatb.2012.02.009.